



Subcell resolution in simplex stochastic collocation for spatial discontinuities



Jeroen A.S. Witteveen^{a,b,*}, Gianluca Iaccarino^a

^a Center for Turbulence Research, Stanford University, Building 500, Stanford, CA 94305-3035, USA

^b Center for Mathematics and Computer Science (CWI), Science Park 123, 1098XG Amsterdam, The Netherlands

ARTICLE INFO

Article history:

Received 26 March 2012

Available online 6 June 2013

Keywords:

Subcell resolution

Finite volume method

Discontinuities

ABSTRACT

Subcell resolution has been used in the Finite Volume Method (FVM) to obtain accurate approximations of discontinuities in the physical space. Stochastic methods are usually based on local adaptivity for resolving discontinuities in the stochastic dimensions. However, the adaptive refinement in the probability space is ineffective in the non-intrusive uncertainty quantification framework, if the stochastic discontinuity is caused by a discontinuity in the physical space with a random location. The dependence of the discontinuity location in the probability space on the spatial coordinates then results in a staircase approximation of the statistics, which leads to first-order error convergence and an under-prediction of the maximum standard deviation. To avoid these problems, we introduce subcell resolution into the Simplex Stochastic Collocation (SSC) method for obtaining a truly discontinuous representation of random spatial discontinuities in the interior of the cells discretizing the probability space. The presented SSC-SR method is based on resolving the discontinuity location in the probability space explicitly as function of the spatial coordinates and extending the stochastic response surface approximations up to the predicted discontinuity location. The applications to a linear advection problem, the inviscid Burgers' equation, a shock tube problem, and the transonic flow over the RAE 2822 airfoil show that SSC-SR resolves random spatial discontinuities with multiple stochastic and spatial dimensions accurately using a minimal number of samples.

© 2013 Elsevier Inc. All rights reserved.

1. Introduction

The notion of subcell resolution in the Finite Volume Method (FVM) originated from Harten [13] to prevent the smearing of contact discontinuities in the solution of hyperbolic conservation laws in the physical space X . It is based on the observation that the location of a discontinuity x_{disc} within a spatial cell X_j can be derived from the computed cell-averaged value \bar{w}_j approximating a flow quantity $u(x)$. In an Essentially Non-Oscillatory (ENO) FVM scheme [12], the ENO reconstructions of $u(x)$ in the cells to the left and the right of the discontinuous cell X_j , $w_{j-1}(x)$ and $w_{j+1}(x)$, are then extended up to an approximation of the discontinuity location x_{disc} in X_j such that their integral matches the cell average \bar{w}_j , see Fig. 1. This allows for resolving discontinuities in the interior of the cells instead of restricting them to the cell face locations. The concept can be extended to multiple spatial dimensions using the dimensional splitting approach.

In contrast, stochastic methods commonly approximate discontinuities in the probability space Ξ using local adaptivity in a multi-element discretization of the stochastic dimensions. These local methods divide the probability space into multiple

* Corresponding author at: Center for Mathematics and Computer Science (CWI), Science Park 123, 1098XG Amsterdam, The Netherlands. Tel.: +31 (0) 20 592 4085.

E-mail addresses: jeroen.witteveen@cwi.nl (J.A.S. Witteveen), jops@stanford.edu (G. Iaccarino).

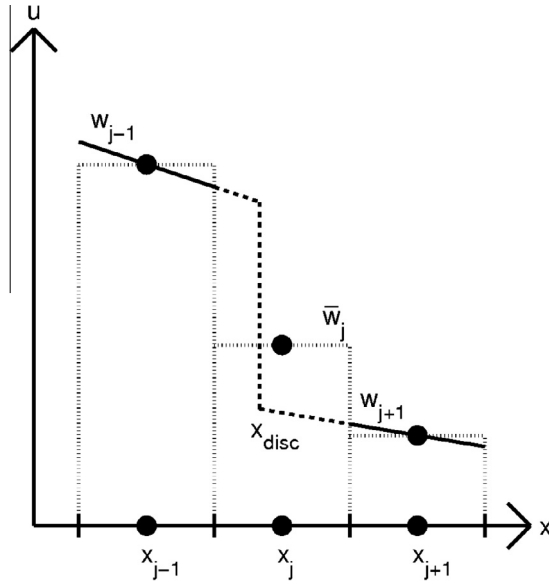


Fig. 1. Subcell resolution in the FVM spatial discretization for $u(x)$ with the extensions of the ENO approximations $w_{j-1}(x)$ and $w_{j+1}(x)$ up to the estimate of the discontinuity location x_{disc} that match the cell average \bar{w}_j .

subdomains comparable to spatial discretizations of the physical space. For instance, multi-element stochastic Galerkin methods [4,19,30] use polynomial chaos expansions [15,37] to approximate the response in each of the cells discretizing the probability space. Non-intrusive alternatives [3,14,18] employ Stochastic Collocation (SC) approaches [5,38] to construct local polynomial interpolations of samples at quadrature points in the cells. These methods commonly use sparse grids of Gauss quadrature rules in hypercube subdomains combined with solution-adaptive refinement measures [20] for resolving nonlinearities. The non-intrusive Simplex Stochastic Collocation (SSC) method [34,35] based on a simplex tessellation of the probability space achieves a robust approximation of discontinuities using a linear interpolation at the jump and ENO-type stencil selection in the SSC-ENO approach [36].

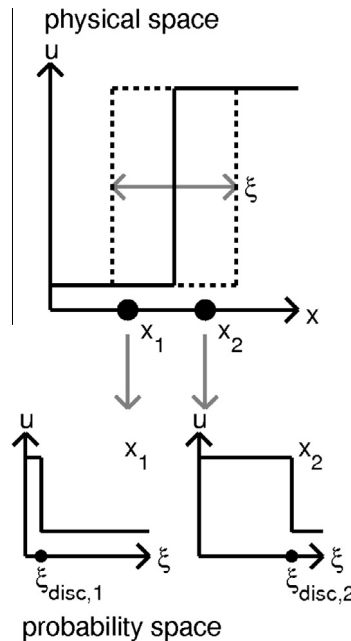


Fig. 2. A step function $u(x)$ with a random jump location $x_{disc} = \xi$ in the physical space results in different discontinuity locations, $\xi_{disc,1}$ and $\xi_{disc,2}$, in the probability space for different spatial points x_1 and x_2 .

However, in problems where the location of a discontinuity in the physical space is random, adaptive refinement in the probability space proves ineffective in the non-intrusive uncertainty quantification framework, see [26,32]. This is not necessarily the case for adaptive intrusive Galerkin projection methods, see for instance [29]. For each point x in the physical space, the spatial discontinuity namely results in a jump at a different location ξ in the probability space, see Fig. 2. Random discontinuity locations also result in staircase approximations for the mean and standard deviation fields that converge with first-order accuracy only. This coincides with an underprediction of the maximum standard deviation as well. Since a non-intrusive stochastic approach is based on the interpolation of samples, the discontinuity does not affect the solution unless it moves across a sampling point in the probability space. At that moment, the solution changes discontinuously and it remains constant in between. This results in the mentioned staircase approximation, while the exact solution can be continuous. This is illustrated in more detail for the example in Section 3.1. Therefore, we introduce the concept of subcell resolution into the SSC-SR method to achieve accurate approximations of random spatial discontinuities in the probability space.

The subcell resolution is obtained by extracting the discontinuity location x_{disc} in the physical space from each of the deterministic simulations for the sampled random parameter values ξ_k . These physical discontinuity locations x_{disc} are interpolated in the stochastic dimensions to derive a relation for the location of the discontinuity ξ_{disc} in the probability space as a function of the spatial coordinate x . In the discontinuous cells, the interpolations $w_j(\xi)$ of the neighboring cells Ξ_j are then extended from both sides up to the predicted discontinuity location ξ_{disc} . This leads to a genuinely discontinuous representation of the jump in the interior of the cells in the probability space, which avoids the underprediction of the standard deviation without the need for linear interpolation and adaptive sampling near the discontinuity. It also avoids the staircase approximation of the statistical moments because of the continuous dependence of the discontinuity location ξ_{disc} in the probability space on the spatial coordinate x . For multiple random parameters, it leads to a multi-dimensional representation of the discontinuous front without the need for dimensional splitting.

Subcell resolution in stochastic methods has also been proposed by Ghosh and Ghanem [16] in the form of basis enrichment in the polynomial chaos expansion. Their approach is, however, based on incorporating *a priori* knowledge about the discontinuity location by selecting appropriate enrichment functions. Abgrall [1,2] and Barth [6] have extended FVM directly to discretize the combined physical and probability spaces using the ENO scheme. We consider here the spatial and stochastic dimensions separately to reduce the dimensionality of the problems. A solution for the staircase approximation of the statistics in case of random spatial discontinuities has also been proposed by Barth [7] using image enhancement postprocessing techniques in the combined discretization of the physical and probability spaces.

The developed SSC-SR method is analyzed in application to a linear advection problem, the inviscid Burgers' equation, a Riemann problem in a shock tube, and the transonic flow over an airfoil. For the inviscid Burgers' equation, a staircase solution of the stochastic Galerkin approach has been reported in [22]. It has been suggested to use additional dissipation to smoothen the steps for a qualitatively better solution. The inviscid Burgers' equation has also been used by Chen et al. [10] and Chantrasmi et al. [8] as a model for the flow through a dual throat nozzle to study random shock wave locations. The inviscid Burgers' equation and the Riemann problem have been considered by Poëtte et al. [23] to demonstrate that their polynomial chaos method based on entropic variables is more precise in discontinuous cases than the stochastic Galerkin method. Both problems have also been used by Tryoen et al. [28] to assess the robustness and the efficiency of their multi-resolution stochastic Galerkin method with upwinding in case of discontinuities in the physical and probability spaces. In transonic airfoil flows, a stair-like solution profile and an underprediction of the standard deviation have been observed by Simon et al. [26] in the region of the shock movement. They conclude that these problems can be alleviated by selecting a sufficiently high number of sampling points with respect to the spatial resolution at the expense of significant computational costs in higher dimensional problems. A non-intrusive stochastic projection method has also been applied to transonic flow over an airfoil by Chassaing and Lucor [9] with randomness in the free-stream conditions. Other transonic airfoil flows have previously been considered in [31,32].

The subcell resolution is introduced in the SSC-SR method in Section 2. The results for the linear advection problem, the inviscid Burgers' equation, the shock tube problem, and the transonic airfoil flow are compared with those of the SSC-ENO method without subcell resolution in Sections 2–6, respectively. The main conclusions are summarized in Section 7.

2. Simplex stochastic collocation with subcell resolution

The subcell resolution in stochastic problems is presented for discontinuities and discontinuous derivatives in combination with a sampling strategy for the resulting SSC-SR algorithm.

2.1. Stochastic problem statement

Consider the following operator equation for the flow quantity $u(\mathbf{x}, t, \xi)$ as function of the spatial and temporal coordinates, $\mathbf{x} \in X \subset \mathbb{R}^{n_x}$ with the spatial dimensionality $n_x \in \{1, 2, 3\}$ and $t \in T \subset \mathbb{R}$, and the vector of n_ξ second-order random parameters $\xi = \{\xi_1, \dots, \xi_{n_\xi}\} \in \Xi$ with the probability distribution $f_\xi(\xi)$ and the parameter space $\Xi \subset \mathbb{R}^{n_\xi}$.

$$\mathcal{L}(\mathbf{x}, t, \xi; u(\mathbf{x}, t, \xi)) = \mathcal{S}(\mathbf{x}, t, \xi), \quad (1)$$

where the operator \mathcal{L} and the source term \mathcal{S} are defined on the domain $X \times T \times \Xi$ with appropriate initial and boundary conditions. The temporal argument t is dropped from here onto shorten the notation. The parameter space Ξ is discretized in the SSC method [34,35] using a tessellation of n_e non-overlapping simplexes Ξ_j , for which holds $\Xi = \bigcup_{j=1}^{n_e} \Xi_j$. Computationally intensive deterministic solutions $v_k(\mathbf{x}) = u(\mathbf{x}, \xi_k)$ of the governing Eq. (1) are calculated using a spatial discretization method for the parameter values that correspond to the n_s sampling points ξ_k at the vertexes of the simplexes Ξ_j . This results in the set of samples $\mathbf{v}(\mathbf{x}) = \{v_1(\mathbf{x}), \dots, v_{n_s}(\mathbf{x})\}$. The response surface for $u(\mathbf{x}, \xi)$ in the probability space is approximated by $w(\mathbf{x}, \xi)$ using a polynomial chaos expansion [15,37] in all simplexes Ξ_j in terms of the basis polynomials $\Psi_{j,i}(\xi)$

$$w_j(\mathbf{x}, \xi) = \sum_{i=0}^{p_j(\mathbf{x})} c_{j,i}(\mathbf{x}) \Psi_{j,i}(\xi), \quad (2)$$

with piecewise polynomial $w(\mathbf{x}, \xi) = w_j(\mathbf{x}, \xi)$ for $\xi \in \Xi_j$ and $p_j(\mathbf{x}) + 1 = (n_\xi + p_j(\mathbf{x}))!/(n_\xi! p_j(\mathbf{x})!)$ the number of expansion terms, where $p_j(\mathbf{x})$ is the local polynomial degree of $w_j(\mathbf{x}, \xi)$ in Ξ_j . The index j of the polynomial degree $p_j(\mathbf{x})$ of the interpolation $w_j(\mathbf{x}, \xi)$ in the simplex Ξ_j in the probability space denotes that $p_j(\mathbf{x})$ can be different for different simplexes Ξ_j in the probability space. In addition, the polynomial degree $p_j(\mathbf{x})$ in one simplex Ξ_j in the probability space can also be different for different points in the spatial discretization of \mathbf{x} depending on the resulting location of the discontinuity in the probability space for that \mathbf{x} . In order to clarify the notation, the subscript k is consistently used for sampling points ξ_k and the subscript j is only used to refer to simplex elements Ξ_j . The way in which the polynomial degree $p_j(\mathbf{x})$ is selected is described in Appendix A. Monomials are used for the basis polynomials $\Psi_{j,i}(\xi)$ in this case and orthogonal polynomials could be used to improve the numerical stability. The coefficients $c_{j,i}(\mathbf{x})$ are determined by interpolating the samples $v_k(\mathbf{x})$ of a stencil $S_j(\mathbf{x}) = \{\xi_{k_{j,0}}, \dots, \xi_{k_{j,N_j(\mathbf{x})}}\}$ of $N_j(\mathbf{x}) + 1$ unique sampling points ξ_k , with $k_{j,l} \in \{1, \dots, n_s\}$ and $l = 0, \dots, N_j(\mathbf{x})$. The first $n_\xi + 1$ sampling points ξ_k of the stencil $S_j(\mathbf{x})$ consist of the vertexes of the simplex Ξ_j and the $N_j(\mathbf{x}) - n_\xi$ other sampling points are vertexes of the surrounding simplexes, see Fig. 3 for an example in a two-dimensional probability space. The interpolation procedure (2) in the probability space is denoted by the interpolation operator \mathcal{I} , for which holds $w(\mathbf{x}, \xi) = \mathcal{I}(\mathbf{v}(\mathbf{x}))$. More details about the stochastic discretization and the initial tessellation before refinements are given in Appendix A.

2.2. Subcell resolution

The sequence of operations in the subcell resolution algorithm is listed below. The subcell resolution is first introduced for a one-dimensional physical space $x \in X$ with $n_x = 1$ and later described for multiple spatial dimensions.

2.2.1. Extraction of discontinuity locations

Assume that $u(x, \xi)$ contains a discontinuity, of which the location $x_{\text{disc}}(\xi)$ in the physical space X is a function of the stochastic dimensions ξ . The samples $\mathbf{v}(x)$ for the flow quantity $u(x, \xi)$ are then used to extract n_s realizations $\mathbf{v}_{\text{disc}} = \{v_{\text{disc}_1}, \dots, v_{\text{disc}_{n_s}}\}$ for the physical discontinuity location $x_{\text{disc}}(\xi)$ at the sampling points ξ_k . This is referred to as the extraction operation \mathcal{E} that returns $\mathbf{v}_{\text{disc}} = \mathcal{E}(\mathbf{v}(x))$ with $v_{\text{disc}_k} = x_{\text{disc}}(\xi_k)$. In Fig. 4(a), an example of the extraction of v_{disc_k} from the sample $v_k(x)$ for the sampling point ξ_k is given for one stochastic dimension ξ . The set of realizations v_{disc_k} for $n_s = 5$ sampling points ξ_k is shown in Fig. 4(b) by the dots in the plot of the discontinuity location $x_{\text{disc}}(\xi)$ in the physical space as function of the random parameter ξ .

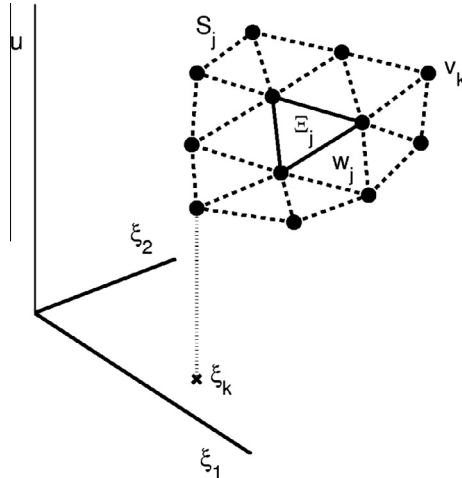


Fig. 3. SSC discretization of a two-dimensional probability space for approximating the response $u(\mathbf{x}, \xi)$ as function of the stochastic dimensions $\xi = \{\xi_1, \xi_2\}$ by the interpolation $w_j(\mathbf{x}, \xi)$ of a stencil $S_j(\mathbf{x})$ of the samples $v_k(\mathbf{x})$ at the sampling points ξ_k for the simplex Ξ_j .

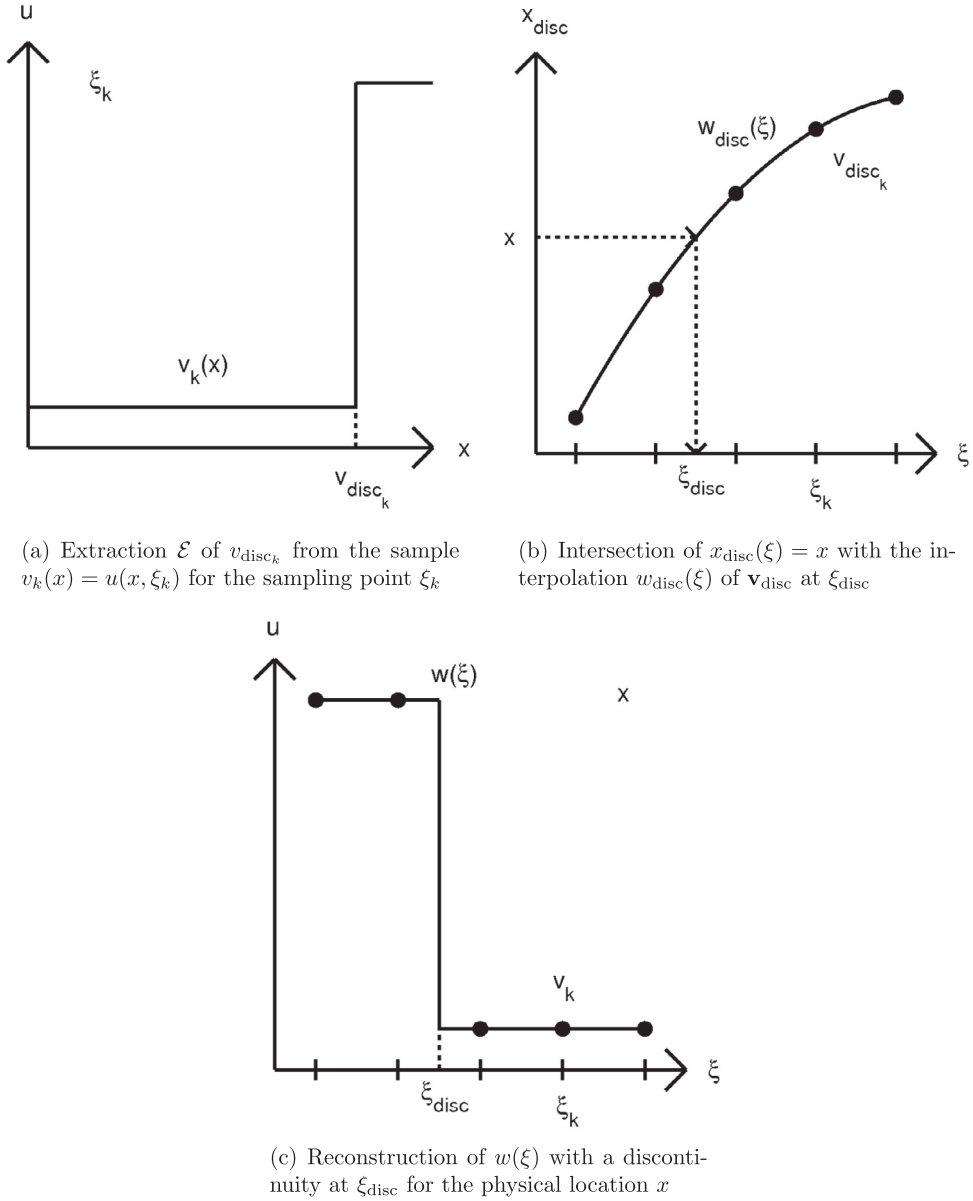


Fig. 4. Example of the subcell resolution approach for a discontinuity in a one-dimensional probability space.

The specific method for the extraction \mathcal{E} of the physical discontinuity locations v_{disc_k} from the deterministic flow fields for the local flow quantity $v_k(x)$ can depend on the type of representation of the discontinuity that is used by the spatial discretization method. The discontinuity locations are explicitly resolved, for example, in subcell resolution FVM discretizations in the physical space and front tracking methods or level set approaches. Shock sensors in hybrid shock capturing methods or adaptive mesh refinement strategies can also be used to identify the discontinuity locations. Otherwise, approaches can be used based on local maxima in the gradient magnitude of the solutions $v_k(x)$, such as the shock detector proposed by Harten [13]. These different extraction operators \mathcal{E} are illustrated in the numerical examples in Sections 2–6 for FVM and front tracking discretizations in physical space.

2.2.2. Interpolation of discontinuity locations

The realizations \mathbf{v}_{disc} for the physical discontinuity location are interpolated over the probability space to the function $w_{disc}(\xi)$ to obtain an approximation of the discontinuity location $x_{disc}(\xi)$ in the physical space as function of the stochastic coordinates ξ , see Fig. 4(b). The piecewise higher-degree polynomial interpolation $w_{disc}(\xi) = \mathcal{I}(\mathbf{v}_{disc})$ is obtained using the interpolation operator \mathcal{I} (2)

$$w_{\text{disc}_j}(\xi) = \sum_{i=0}^{P_{\text{disc}_j}} c_{\text{disc}_{j,i}} \Psi_{j,i}(\xi), \quad (3)$$

with $w_{\text{disc}}(\xi) = w_{\text{disc}_j}(\xi)$ for $\xi \in \Xi_j$ and the $P_{\text{disc}_j} + 1$ coefficients $c_{\text{disc}_{j,i}}$ determined by the interpolation of a stencil S_{disc_j} of the realizations v_{disc_k} .

2.2.3. Intersection with spatial point x

The location of the discontinuity in the probability space for a certain point x in the physical space can then be described by the hypersurface $\Xi_{\text{disc}}(x) \subset \Xi$. This discontinuous hypersurface $\Xi_{\text{disc}}(x)$ in the probability space is given by the intersection of $w_{\text{disc}}(\xi)$ with the hyperplane $x_{\text{disc}}(\xi) = x$, such that for all points $\xi_{\text{disc}} \in \Xi_{\text{disc}}(x)$ holds $w_{\text{disc}}(\xi_{\text{disc}}) = x$. Therefore, Ξ_{disc} contains all combinations of random parameter values ξ_{disc} for which the discontinuity in the physical space is predicted to be located at x . In the example of Fig. 4(b) with a one-dimensional probability space, the set $\Xi_{\text{disc}}(x)$ consists of a single point ξ_{disc} for which $w_{\text{disc}}(\xi_{\text{disc}}) = x$. For multiple random parameters ξ , the intersection $\Xi_{\text{disc}}(x)$ of $w_{\text{disc}}(\xi)$ with $x_{\text{disc}}(\xi) = x$ is a piecewise higher-degree function that is able to capture nonlinear curvatures of discontinuous hypersurfaces in the probability space.

2.2.4. Identification of discontinuous simplexes

The parameter space Ξ is next divided into two subdomains $\Xi^-(x)$ and $\Xi^+(x)$ separated by $\Xi_{\text{disc}}(x)$, for which holds $w_{\text{disc}}(\xi^-) < x$ with $\xi^- \in \Xi^-(x)$, $w_{\text{disc}}(\xi^+) > x$ with $\xi^+ \in \Xi^+(x)$, and $\Xi = \Xi^-(x) \cup \Xi^+(x)$. The discontinuous simplexes Ξ_j that contain $\Xi_{\text{disc}}(x)$ are identified by

$$w_{\text{disc}_j}(\xi^-) < x \text{ for some } \xi^- \in \Xi_j \wedge w_{\text{disc}_j}(\xi^+) > x \text{ for some } \xi^+ \in \Xi_j. \quad (4)$$

2.2.5. Reconstruction of discontinuous response surface

The interpolation $w_j(x, \xi)$ (2), in the simplexes Ξ_j that satisfy (4), is replaced by a discontinuous representation of the response surface $u(x, \xi)$. To that end, the simplex Ξ_j is divided into two regions $\Xi_j^-(x) \subset \Xi^-(x)$ and $\Xi_j^+(x) \subset \Xi^+(x)$ with $\Xi_j = \Xi_j^-(x) \cup \Xi_j^+(x)$. The interpolation $w_j(x, \xi)$ in $\Xi_j^-(x)$ is replaced by the approximation $w_j^-(x, \xi) = w_{i^-}(x, \xi)$ of the simplex Ξ_{i^-} closest to Ξ_j for which holds $\Xi_{i^-} \subset \Xi^-$. The nearest cell Ξ_{i^-} is defined as the simplex that has the most vertexes ξ_k in common with Ξ_j and that has the highest polynomial degree p_{i^-} out of these cells. The region $\Xi_j^+(x)$ is assigned the different interpolation $w_j^+(x, \xi) = w_{i^+}(x, \xi)$ of the nearest simplex $\Xi_{i^+} \subset \Xi^+$ with $i^-, i^+ \in \{1, \dots, n_e\}/j$. The notation is illustrated in Fig. 5 for the case of a two-dimensional probability space. This leads for SSC-SR to the response surface approximation $w(x, \xi)$ given by

$$w(x, \xi) = \begin{cases} w_j(x, \xi), & \xi \in \Xi_j, \quad \Xi_j \subset \Xi^- \vee \Xi_j \subset \Xi^+, \\ w_j^-(x, \xi), & \xi \in \Xi_j^-, \quad \Xi_j \not\subset \Xi^- \wedge \Xi_j \not\subset \Xi^+, \\ w_j^+(x, \xi), & \xi \in \Xi_j^+, \quad \Xi_j \not\subset \Xi^- \wedge \Xi_j \not\subset \Xi^+, \end{cases} \quad (5)$$

which is discontinuous at the predicted discontinuity location $\Xi_{\text{disc}}(x)$, see Fig. 4(c) for the result in the one-dimensional probability space. Integrating $w(x, \xi)$ over the parameter space Ξ yields an approximation of the statistical moments of u at the spatial point x . In order to obtain the spatial fields for the mean $\mu_w(x)$ and the standard deviation $\sigma_w(x)$, the approximations $\Xi_{\text{disc}}(x)$ and $w(x, \xi)$ are constructed for each point x in the spatial discretization of X .

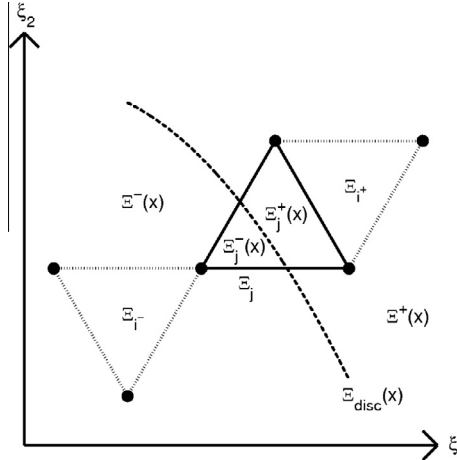


Fig. 5. Division of the simplex Ξ_j in the two-dimensional parameter space Ξ by the discontinuous front $\Xi_{\text{disc}}(x)$ into $\Xi_j^-(x)$ and $\Xi_j^+(x)$ with the nearest simplexes Ξ_{i^-} and Ξ_{i^+} in $\Xi^-(x)$ and $\Xi^+(x)$, respectively.

2.2.6. Multiple spatial dimensions

For $n_x \in \{2, 3\}$, the location of the discontinuity is described by the discontinuous surface $X_{\text{disc}}(\xi) \subset X$ in the physical space. Therefore, instead of using the discontinuity location $x_{\text{disc}}(\xi)$, the signed Euclidean distance $d_{\text{disc}}(\mathbf{x}, \xi)$ from the discontinuity $X_{\text{disc}}(\xi)$ to a point \mathbf{x} in the physical space is parameterized for $n_x > 1$. The sign is obtained using the cross product, at the point on the discontinuity $X_{\text{disc}}(\xi)$ closest to \mathbf{x} , between the tangent of $X_{\text{disc}}(\xi)$ and the vector to \mathbf{x} , which is illustrated in Section 6 for the RAE 2822 airfoil. The subcell resolution method is then equal to the approach presented in this section for $n_x = 1$ by substituting $d_{\text{disc}}(\mathbf{x}, \xi)$ for $x_{\text{disc}}(\xi)$ and the location of the discontinuous hypersurface $\Xi_{\text{disc}}(\mathbf{x})$ is given by $d_{\text{disc}}(\mathbf{x}, \xi) = 0$. Since $d_{\text{disc}}(\mathbf{x}, \xi)$ depends on the reference point \mathbf{x} in the physical space, the realizations $v_{\text{disc}_k}(\mathbf{x})$ of $d_{\text{disc}}(\mathbf{x}, \xi)$ and the interpolation $w_{\text{disc}}(\mathbf{x}, \xi)$ become a function of \mathbf{x} , such that the interpolation step $w_{\text{disc}}(\mathbf{x}, \xi) = \mathcal{I}(\mathbf{v}_{\text{disc}}(\mathbf{x}))$ is also repeated for each \mathbf{x} in the spatial discretization. For a one-dimensional physical space, $r = 1$, the distance reduces to $d_{\text{disc}}(\mathbf{x}, \xi) = x_{\text{disc}}(\xi) - x$ such that parameterizing the discontinuity location $x_{\text{disc}}(\xi) = X_{\text{disc}}(\xi)$ is sufficient, which is independent of x . If multiple discontinuities are present in the spatial field of $u(x, \xi)$ then the subcell resolution algorithm is applied to each physical discontinuity. A non-monotonic function for $w_{\text{disc}}(\mathbf{x}, \xi)$ also results in multiple discontinuities in $w(x, \xi)$ at certain values of x .

2.3. Sampling strategy

At physical points x where the hypersurface $\Xi_{\text{disc}}(x)$ is located close to the boundary of the parameter space Ξ , no simplexes Ξ_i may lie entirely in the region on one side of $\Xi_{\text{disc}}(x)$. For instance, Ξ^- might not contain any simplexes Ξ_i^- for updating the interpolation $w_j^-(x, \xi)$ to $w_{i^-}(x, \xi)$ in $\Xi_j^-(x)$ of the simplex Ξ_j that contains $\Xi_{\text{disc}}(x)$. Such an example is given in Fig. 6 for the initial number of $n_s = 5$ samples in a two-dimensional probability space. In that case, a constant function is used for $w_j^-(x, \xi)$. The constant value for $w_j^-(x, \xi)$ is the arithmetic average of the samples $v_k(x)$ at the vertexes of Ξ_j in Ξ_j^- . The treatment of discontinuous derivatives in the response surface and, in that case, the linear reconstruction of $w_j^-(x, \xi)$ when $\Xi_{\text{disc}}(x)$ is located close to the boundary of Ξ are discussed in Appendix B. In any other cases, the interpolation $w_j(x, \xi)$ (2) is simply retained.

The potentially constant approximation of $w_j^-(x, \xi)$ near the boundary of Ξ , or the linear function in case of a discontinuous derivative, is the lowest local polynomial degree of the otherwise higher-degree response surface approximation $w(x, \xi)$. Therefore, a sampling strategy is used that reduces the size of these regions in the parameter space Ξ . To that end, the following refinement measure e_{\max_j} , based on [34], is used for the simplexes Ξ_j in the refinement procedure

$$e_{\max_j} = \max_{x \in X} e_j(x), \quad e_j(x) = \bar{\Omega}_j \bar{\Xi}_j^{2O_j(x)}, \quad (6)$$

with the probability $\bar{\Omega}_j$ contained by Ξ_j , the normalized volume of Ξ_j in the parameter space Ξ , and the local estimated order of convergence $O_j(x)$ given by

$$\bar{\Omega}_j = \int_{\Xi_j} f_\xi(\xi) d\xi, \quad \bar{\Xi}_j = \frac{1}{\Xi} \int_{\Xi_j} d\xi, \quad O_j(x) = \frac{p_j(x) + 1}{n_\xi}, \quad (7)$$

where $\Xi = \int_{\Xi} d\xi$. The polynomial degree $p_j(x)$ of the discontinuous simplexes Ξ_j is defined as the probabilistically weighted average of the polynomial degrees over its two subdomains Ξ_j^- and Ξ_j^+

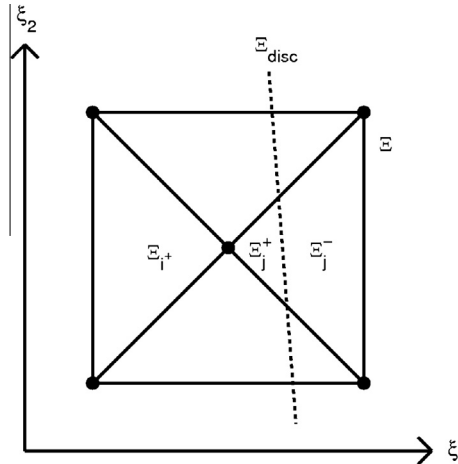


Fig. 6. Example of the initial discretization of a two-dimensional parameter space Ξ with $n_s = 5$, where no simplex Ξ_i^- is available to update the interpolation $w_j^-(x, \xi)$ in $\Xi_j^-(x)$.

$$p_j(x) = \frac{1}{\bar{\Omega}_j} \left[\int_{\Xi_j^-} p_j^-(x) f_\xi(\xi) d\xi + \int_{\Xi_j^+} p_j^+(x) f_\xi(\xi) d\xi \right], \quad (8)$$

with $p_j^-(x)$ and $p_j^+(x)$ the polynomial degrees of $w_j^-(x, \xi)$ and $w_j^+(x, \xi)$ in Ξ_j^- and Ξ_j^+ , respectively. The refinement focuses automatically on the simplexes Ξ_j with a low interpolation degree $p_j(x)$ weighted by the local probability $\bar{\Omega}_j$. The low values of $p_j(x)$ occur near the boundary of Ξ at certain x -locations, instead of at the discontinuity $\Xi_{\text{disc}}(x)$, as is demonstrated in the numerical examples. The response surface approximation $w_{\text{disc}}(x, \xi)$ for the discontinuity location $x_{\text{disc}}(\xi)$ can be included in the refinement measure (6) through p_{disc} to resolve nonlinearities in $w_{\text{disc}}(x, \xi)$ as well.

2.4. SSC-SR algorithm summary

The SSC-SR algorithm replaces the linear approximation $w_j(x, \xi)$ of the SSC-ENO method [36] in the simplexes Ξ_j that contain a spatial discontinuity by a discontinuous representation. The algorithm contains the following five steps, which are valid in probability spaces of arbitrary dimensionality n_ξ and not limited to simplex discretizations of the stochastic dimensions:

1. Extract the realizations $v_{\text{disc}_k} = \mathcal{E}(v_k(x))$ for the discontinuity location $x_{\text{disc}}(\xi)$ in the physical space X from the samples $v_k(x)$ for the response $u(x, \xi)$ at the sampling points ξ_k with $k = 1, \dots, n_s$;
2. Interpolate the realizations \mathbf{v}_{disc} to the function $w_{\text{disc}}(\xi) = \mathcal{I}(\mathbf{v}_{\text{disc}})$ approximating the discontinuity location $x_{\text{disc}}(\xi)$ in the physical space as function of the stochastic coordinates ξ ;
3. Intersect the function $w_{\text{disc}}(\xi)$ with the hyperplane $x_{\text{disc}}(\xi) = x$ to find the location of the discontinuous hypersurface $\Xi_{\text{disc}}(x) \subset \Xi$ in the probability space for the spatial point x ;
4. Identify the simplexes Ξ_j that contain the discontinuous hypersurface $\Xi_{\text{disc}}(x)$ using (4);
5. Update the interpolations $w_j^-(x, \xi)$ and $w_j^+(x, \xi)$ in each of the discontinuous simplexes Ξ_j on both sides of $\Xi_{\text{disc}}(x)$ by the approximations $w_{i^-}(x, \xi)$ and $w_{i^+}(x, \xi)$ of the nearest simplexes Ξ_{i^-} and Ξ_{i^+} in the regions $\Xi^-(x)$ and $\Xi^+(x)$ of the parameter space Ξ on either side of $\Xi_{\text{disc}}(x)$, respectively, which results in the response surface approximation $w(x, \xi)$ given by (5).

The spatial fields of the statistical moments are obtained by repeating steps 3 to 5 for the points x in the spatial discretization of X and integrating $w(x, \xi)$ over the parameter space Ξ . In multi-dimensional physical spaces X , the signed Euclidean distance $d_{\text{disc}}(\mathbf{x}, \xi)$ between the point \mathbf{x} and the discontinuity $X_{\text{disc}}(\xi) \subset X$ in the physical space is parameterized, instead of $x_{\text{disc}}(\xi)$, and steps 1 and 2 are also repeated. If no simplexes Ξ_{i^-} or Ξ_{i^+} are available at an x -location for certain simplexes Ξ_j , then a constant or linear function for $w_j^-(x, \xi)$ or $w_j^+(x, \xi)$ is used for discontinuities or discontinuous derivatives, respectively, as described in Section 2.3 and Appendix B. The extraction \mathcal{E} of step 1 is assumed to be attainable as is shown for the numerical examples in the following sections, which consider regular perturbation problems without topological changes of the discontinuities.

Subcell resolution is based on the sequential application of the same interpolation algorithm \mathcal{I} to two different response surface approximation problems. The first one is for representing the discontinuity location $w_{\text{disc}}(\xi) = \mathcal{I}(\mathbf{v}_{\text{disc}})$ and the second one for the response itself $w(x, \xi) = \mathcal{I}(\mathbf{v}(x))$. This requires the implementation of only one interpolation algorithm, which can be a less complex one than the simplex discretization used here. It is then relatively straightforward to implement the subcell resolution steps summarized above into the interpolation method for random vectors ξ with more than two dimensions and multidimensional spatial vectors \mathbf{x} . The simplex discretization is also formulated and implemented here for arbitrary stochastic dimensionality.

3. Linear advection equation

The application of the SSC-SR method to a linear advection problem with discontinuous initial conditions is considered in multiple stochastic and physical dimensions. The results are compared to those of the SSC-ENO approach and Monte Carlo (MC) simulation. The linear advection equation in two spatial dimensions for the convected quantity $u(x, y, t)$ is

$$\frac{\partial u}{\partial t} + a \frac{\partial u}{\partial x} + b \frac{\partial u}{\partial y} = 0, \quad (9)$$

with the advection velocities a and b in the x and y -directions, respectively. The initial conditions are given by

$$u(x, y, 0) = H((x - x_0) + (y - y_0)) = \begin{cases} 0, & x + y < x_0 + y_0, \\ 1, & x + y \geq x_0 + y_0, \end{cases} \quad (10)$$

where H is the Heaviside step function, and x_0 and y_0 describe the initial discontinuity location. The analytical solution of (9) and (10) is $u(x, y, t) = H((x - x_0 - at) + (y - y_0 - bt))$.

3.1. Random advection velocity a

Randomness is first considered in the advection velocity a , given by a uniform distribution on the interval $\mathcal{U}(-0.5; 0.5)$, with one spatial coordinate x and a deterministic value for the initial discontinuity location $x_0 = 0$. The initial condition and the deterministic solution at $t = 1$ are shown in Fig. 7(a) for $a = 0.5$. The randomness in a leads to a random discontinuity location x_{disc} in the physical space with $x_{\text{disc}} = a$ at $t = 1$. The combination with the variability in x_0 of Fig. 7(b) is considered in Section 3.2.

The resulting profiles for the mean $\mu_u(x)$ and standard deviation $\sigma_u(x)$ of u are given in Figs. 8 and 9 for SSC-ENO and SSC-SR. Uniform, or volumetric, sampling is used in this example for both approaches based on the refinement measure $\bar{\Xi}_j$. The sampling strategy of Section 2.3 is explored for the other test cases. In Fig. 8(a), the SSC-ENO method clearly gives a staircase approximation of the mean $\mu_u(x)$ with the number of steps equal to the number of sampling points $n_s = \{3, 5, 33\}$. The results with the increasing number of smaller discontinuities approach the converged linear MC solution obtained with $n_{\text{mc}} = 5 \cdot 10^4$ samples. The equidistant steps occur when the spatial discontinuity crosses one of the uniformly spaced sampling points in the one-dimensional probability space. The staircase behavior is, therefore, typical for non-intrusive methods and not specific to SSC-ENO only. It would even appear in the MC solution at an inadequate number of samples of $n_{\text{mc}} < n_x$, with n_x the spatial resolution of $n_x = 1 \cdot 10^3$ points used here. In contrast, SSC-SR achieves a continuous solution for $\mu_u(x)$ in Fig. 8(b), which is already converged to the MC result for $n_s = 3$ and $n_s = 5$ samples.

The staircase approximation of SSC-ENO and the converged continuous solution of SSC-SR can also be observed in Fig. 9 for $\sigma_u(x)$. The standard deviation of SSC-ENO converges from below to the MC maximum of $\sigma_{u_{\text{max}}} = 0.500$ at $x = 0$. A zoom of $\sigma_u(x)$ on the interval $x \in [0; 0.2]$, in Fig. 10, reveals that for $n_s = 33$ samples SSC-ENO still underestimates the maximum standard deviation with $\sigma_{u_{\text{max}}} = 0.495$. It also shows the truly continuous solution of SSC-SR for $\sigma_u(x)$ with $n_s = 3$.

The behavior of the SSC-ENO and SSC-SR solutions can be understood by inspecting the response surface of u in the probability space as function of the random parameter a for an arbitrary x -location, $x = 0.1$, in Fig. 11. The randomness in the step location x_{disc} in the physical space appears in the MC response surface in the probability space for $x = 0.1$ as a discontinuity at $a_{\text{disc}} = 0.1$. SSC-ENO results in a linear interpolation of the samples at the jump, which converges only slowly with the increasing number of samples $n_s = 3$ and $n_s = 5$. The actual location of the discontinuity in between two samples is, therefore, not reflected in the SSC-ENO approximation, which leads to the plateaus in the solutions for $\mu_u(x)$ and $\sigma_u(x)$.

On the contrary, SSC-SR gives a sharp representation of the jump in the discontinuous cell. It extrapolates the approximations in the adjacent cells for $n_s = 5$ up to the estimate of the discontinuity location a_{disc} . For $n_s = 3$, the approximation to the right of the discontinuity is a constant function through the rightmost sample at $a = 0.5$, because in that case the discontinuous cell has no neighboring cell to the right. This corresponds to the exact piecewise constant solution of the linear advection equation, which will not be the case for the nonlinear problems in the next sections.

The location of the discontinuity a_{disc} in the probability space is estimated by SSC-SR as shown in Fig. 12 for $n_s = \{3, 5\}$. The closed circles denote the realizations $v_{\text{disc}_k} = x_0 + a_k t$ of the discontinuity location x_{disc} in the physical space for the deterministic solutions at the sampling points a_k . The interpolation $w_{\text{disc}}(a)$ of the linear relation between x_{disc} and a is exact for $n_s = 3$. For the example of Fig. 11 at $x = 0.1$, the discontinuity location $a_{\text{disc}} = 0.1$ in the probability space results from the intersection of $w_{\text{disc}}(a)$ with the horizontal line $x_{\text{disc}} = 0.1$.

3.2. Random advection velocity a and initial discontinuity location x_0

The additional randomness in the initial discontinuity location x_0 is described by a uniform distribution $\mathcal{U}(-0.2; 0.2)$, which is uncorrelated with the probability distribution of a . The effect of the variation in x_0 was shown in Fig. 7(b) in terms of the deterministic solution for $x_0 = 0.2$ and $a = 0.5$. The results for the two-dimensional probability space are given in

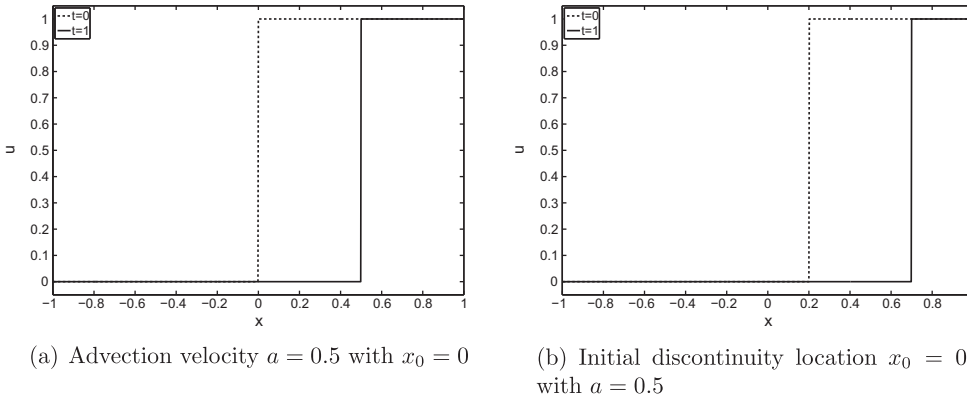


Fig. 7. Initial conditions and deterministic solutions at $t = 1$ for the linear advection equation in one spatial dimension.

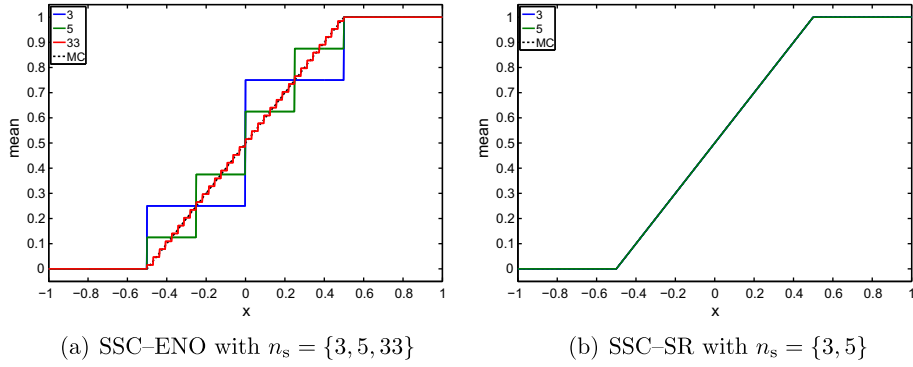


Fig. 8. Mean $\mu_u(x)$ of u for the linear advection equation in one spatial dimension with the random advection velocity a .

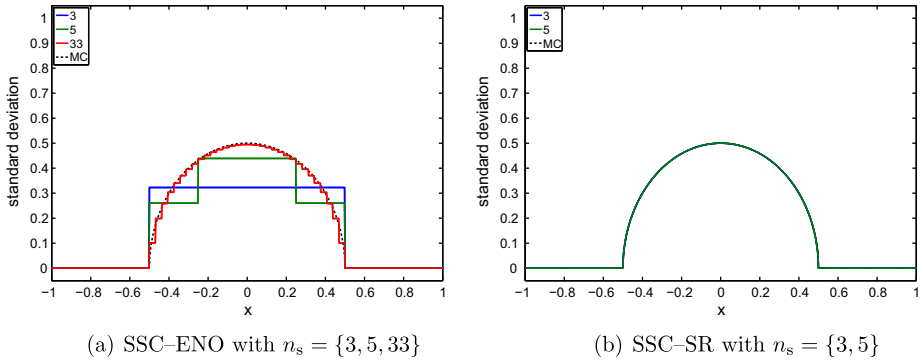


Fig. 9. Standard deviation $\sigma_u(x)$ of u for the linear advection equation in one spatial dimension with the random advection velocity a .

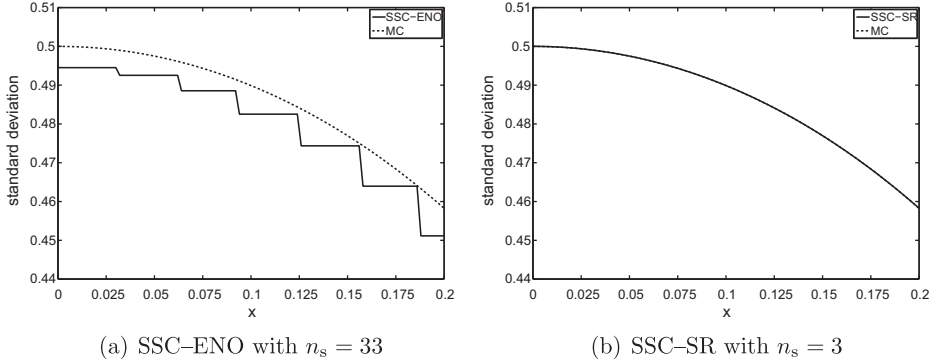


Fig. 10. Zoom of the standard deviation $\sigma_u(x)$ of u on $x \in [0, 0.2]$ for the linear advection equation in one spatial dimension with the random advection velocity a .

Fig. 13 in the form of the mean $\mu_u(x)$, and the 90% and 100% probability intervals for SSC-ENO with $n_s = 33$ and SSC-SR with $n_s = 5$. SSC-ENO gives again a staircase approximation, also for the 90% interval representation. The steps are more irregular because the sampling points in two stochastic dimensions are no longer equidistant. The SSC-SR result already matches the MC solution for both the mean and the intervals at the initial number of $n_s = 5$ samples for discretizing the two-dimensional probability space. At certain x -locations the mean $\mu_u(x)$ lies outside the 90% quantiles because of the nonlinearity of the response surface.

The two-dimensional response surface approximations of SSC-ENO and SSC-SR are visualized in Figs. 14 and 15 for $x = 0.1$. The exact solution for the response of u as function of the random parameters a and x_0 is given in Fig. 14(a). It is a piecewise constant function with a diagonal discontinuity, because of the impact of both a and x_0 on the discontinuity location in the physical space. Fig. 14(b) shows the simplex tessellation of SSC-ENO for $n_s = 33$ and the piecewise linear interpolation of the samples at the discontinuity.

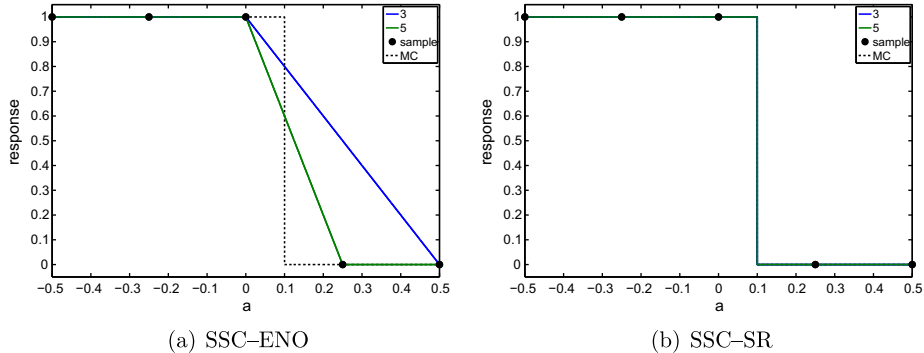


Fig. 11. Response surface approximations for u at $x = 0.1$ with $n_s = \{3, 5\}$ samples as function of the random advection velocity a for the linear advection equation in one spatial dimension.

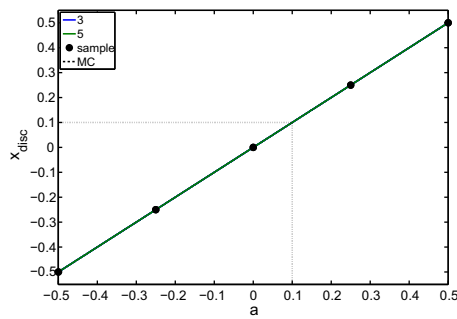


Fig. 12. Response surface approximation w_{disc} for the physical discontinuity location x_{disc} as function of the random advection velocity a by SSC-SR with $n_s = \{3, 5\}$ samples for the linear advection equation in one spatial dimension.

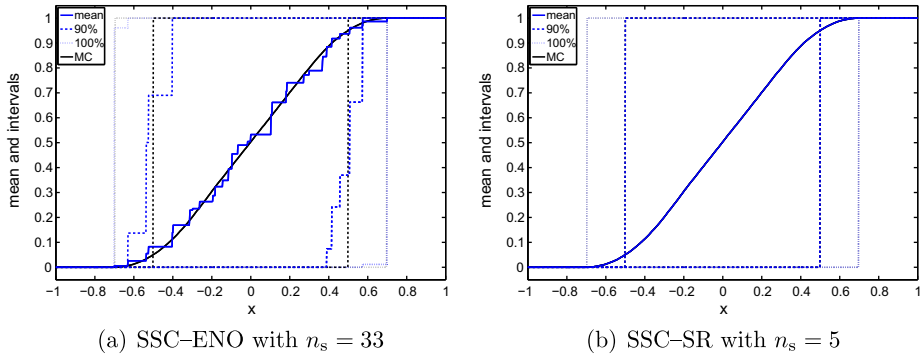


Fig. 13. Mean $\mu_u(x)$, and 90% and 100% probability intervals of u for the linear advection equation in one spatial dimension with the random advection velocity a and initial discontinuity location x_0 .

The SSC-SR method leads to a multi-dimensional representation of the discontinuity in Fig. 15(a) that matches the exact response surface for $n_s = 5$. The jump position is found by constructing the response surface $w_{\text{disc}}(a, x_0)$ for the discontinuity location x_{disc} in the physical space as function of a and x_0 shown in Fig. 15(b), in which a different axes orientation is used for clarity of the figure. The discontinuous front in the a - x_0 plane for $x = 0.1$ is given by the intersection of the response surface $w_{\text{disc}}(a, x_0)$ with the horizontal plane through $x_{\text{disc}} = 0.1$. The approximation of u in the continuous cell at low values of a is then extended into the discontinuous cells up to the estimated discontinuity location. On the other side of the step, the response surface approximation in the discontinuous cells is obtained by a constant interpolation through the two sampling points at $a = 0.5$, since no continuous cell is available in that region for the discretization with $n_s = 5$ samples.

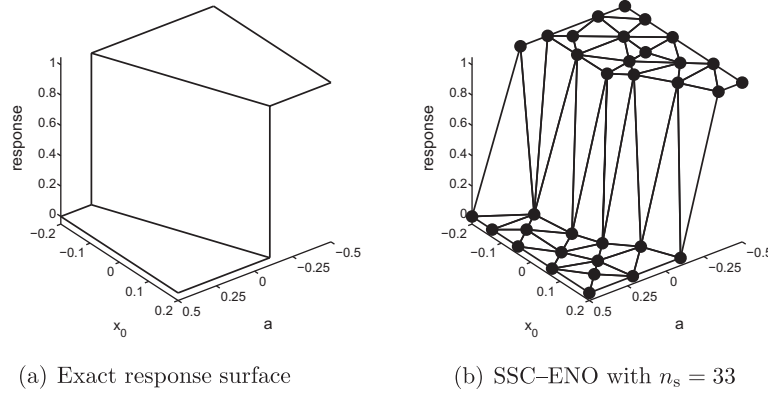


Fig. 14. Response surface of u at $x = 0.1$ as function of the random advection velocity a and initial discontinuity location x_0 for the linear advection equation in one spatial dimension.

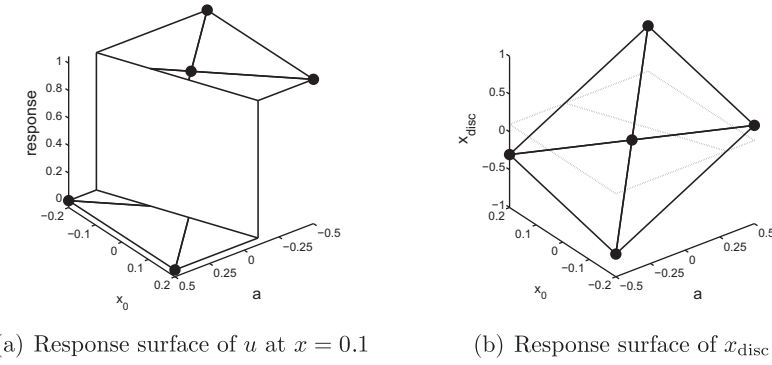


Fig. 15. Response surface approximations as function of the random advection velocity a and initial discontinuity location x_0 by SSC-SR with $n_s = 5$ samples for the linear advection equation in one spatial dimension.

3.3. Higher-dimensional probability spaces

The advection velocity a is decomposed into a summation of n_a random parameters a_i to obtain higher-dimensional probability spaces than in the previous paragraph

$$a = \sum_{i=1}^{n_a} a_i, \quad a_i = \mathcal{U}\left(-\frac{0.5}{n_a}, \frac{0.5}{n_a}\right), \quad (11)$$

such that $a \in [-0.5; 0.5]$. The dimensionality of the problem is then equal to the number of random parameters n_a with the deterministic initial condition $x_0 = 0$. The mean μ_u and standard deviation σ_u at $x = 0.1$ are given in Tables 1 and 2 up to $n_a = 5$ dimensions for SSC-SR with the initial number of samples $n_{s_{\text{init}}}$, MC with the same number of samples, and the MC reference solution with $n_{mc} = 5 \cdot 10^4$. It shows that SSC-SR continues to match the reference results exactly also for discontinuities in the higher-dimensional probability spaces. Therefore, the effectiveness of the subcell resolution approach does, in principle, not depend on the dimensionality of this problem up to $n_a = 5$. The MC solution with the same number of samples

Table 1

Mean μ_u of SSC-SR compared to MC and its reference solution for the linear advection equation in one spatial dimension with the higher-dimensional random advection velocity a .

n_a	$n_{s_{\text{init}}}$	Reference	SSC-SR	MC
1	3	$6.000 \cdot 10^{-1}$	$6.000 \cdot 10^{-1}$	$6.667 \cdot 10^{-1}$
2	5	$6.830 \cdot 10^{-1}$	$6.830 \cdot 10^{-1}$	$8.000 \cdot 10^{-1}$
3	9	$7.181 \cdot 10^{-1}$	$7.181 \cdot 10^{-1}$	$7.778 \cdot 10^{-1}$
4	17	$7.480 \cdot 10^{-1}$	$7.480 \cdot 10^{-1}$	$8.235 \cdot 10^{-1}$
5	33	$7.756 \cdot 10^{-1}$	$7.756 \cdot 10^{-1}$	$8.182 \cdot 10^{-1}$

Table 2

Standard deviation σ_u of SSC-SR compared to MC and its reference solution for the linear advection equation in one spatial dimension with the higher-dimensional random advection velocity a .

n_a	$n_{s_{\text{init}}}$	Reference	SSC-SR	MC
1	3	$4.899 \cdot 10^{-1}$	$4.899 \cdot 10^{-1}$	$4.714 \cdot 10^{-1}$
2	5	$4.653 \cdot 10^{-1}$	$4.653 \cdot 10^{-1}$	$4.000 \cdot 10^{-1}$
3	9	$4.499 \cdot 10^{-1}$	$4.499 \cdot 10^{-1}$	$4.157 \cdot 10^{-1}$
4	17	$4.341 \cdot 10^{-1}$	$4.341 \cdot 10^{-1}$	$3.812 \cdot 10^{-1}$
5	33	$4.172 \cdot 10^{-1}$	$4.172 \cdot 10^{-1}$	$3.857 \cdot 10^{-1}$

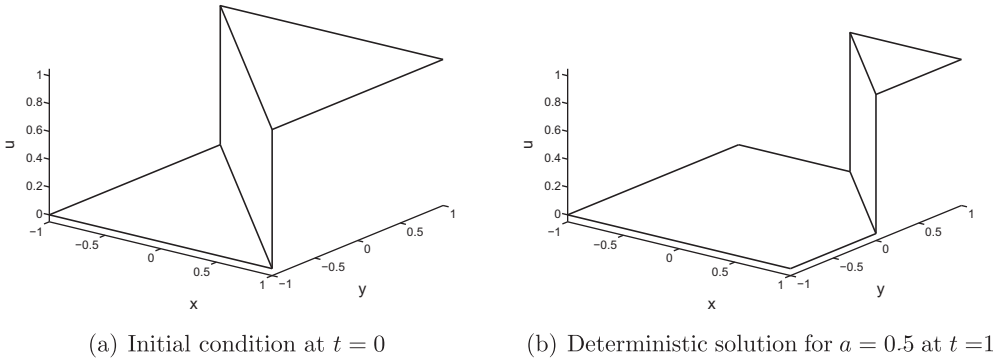


Fig. 16. Initial condition and deterministic solution for the linear advection equation in two spatial dimensions.

is less accurate with an error up to 10% also in higher dimensions. The increase of the initial samples $n_{s_{\text{init}}}$ can further be reduced, for instance, to a linear growth by omitting the samples at the vertexes of the parameter space Ξ as proposed in [34].

3.4. Multi-dimensional physical space

The advection problem is considered in a two-dimensional physical space with fully correlated random advection velocities, $a = b = \mathcal{U}(-0.5; 0.5)$, and deterministic initial conditions $x_0 = y_0 = 0$. The solution of the deterministic problem for $a = 0.5$ is given in Fig. 16 together with the initial condition at $t = 0$. The random discontinuity location leads to the mean $\mu_u(x, y)$ and standard deviation $\sigma_u(x, y)$ fields shown in Figs. 17 and 18 for SSC-ENO with $n_s = 9$ and SSC-SR with $n_s = 3$. Also in multiple spatial dimensions, the SSC-SR method avoids the staircase profile of SSC-ENO in a continuous solution that is identical to the MC result (not shown). Since the problem contains more than one spatial dimension, the signed minimum distance d_{disc} between the discontinuity and a point (x, y) in the physical space is parameterized, instead of the discontinuity location x_{disc} . In this analytical problem, the distance is given by $d_{\text{disc}} = \frac{1}{2}\sqrt{2}((a - x) + (b - y))$. Since d_{disc} depends on x and y , the construction of the response surface for d_{disc} is repeated for each of the 100×100 points in the spatial grid used here.

4. Inviscid Burgers' equation

The Burgers' equation is considered to examine the performance of the SSC-SR method for nonlinear shock speeds and discontinuous derivatives in the response surface. The inviscid Burgers' equation for the velocity $u(x, t)$ in one spatial dimension is given by

$$\frac{\partial u}{\partial t} + u \frac{\partial u}{\partial x} = 0. \quad (12)$$

The initial conditions on the domain $x \in [-1, 1]$ consist here of three uniform regions

$$u(x, 0) = \begin{cases} u_0, & -1 \leq x < -0.5, \\ -0.5, & -0.5 \leq x < x_0, \\ 0.5, & x_0 \leq x \leq 1, \end{cases} \quad (13)$$

with two random parameters describing the initial discontinuity location $x_0 = \mathcal{U}(-0.2; 0.2)$ and the initial value $u_0 = \mathcal{U}(1; 1.5)$. The deterministic problems are solved numerically using a second-order front tracking method [33], which discretizes rarefaction fans by a series of n_f characteristic waves. The shock speed is then updated after every interaction

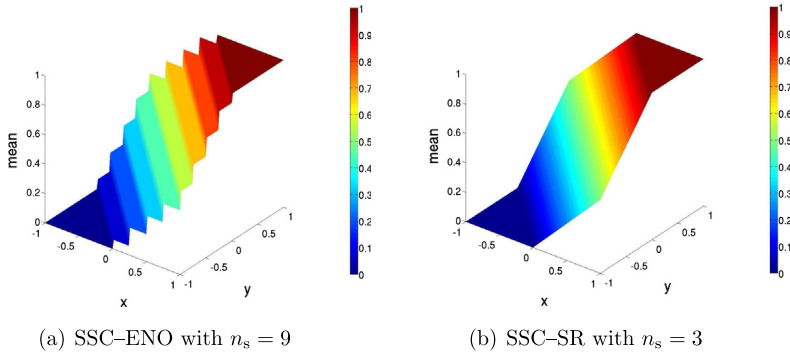


Fig. 17. Mean $\mu_u(x,y)$ of u for the linear advection equation in two spatial dimensions with the random advection velocities a and b .

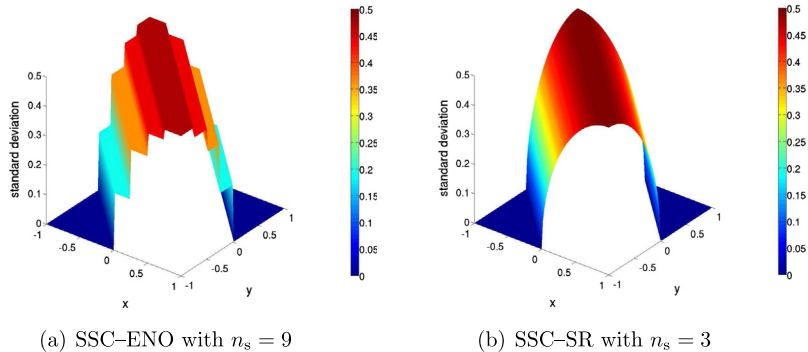


Fig. 18. Standard deviation $\sigma_u(x,y)$ of u for the linear advection equation in two spatial dimensions with the random advection velocities a and b .

with a characteristic wave using a local Riemann solver. It resolves discontinuous phenomena as genuine discontinuities, however, there is a numerical error in its location after it interacts with a continuous wave.

4.1. Random initial discontinuity location x_0

The front tracking solution in the space-time plane up to $t = 1$ is given in Fig. 19 for the extreme values of x_0 with $u_0 = 1.5$. It shows the interaction of the shock wave with the discretization of the rarefaction fan and the resulting curved shock path for $n_f = 20$. The initial conditions and the deterministic solutions for u at $t = 1$ are shown in Fig. 20 for $x_0 = \{-0.2; 0; 0.2\}$ with $n_f = 100$. The initial discontinuity location x_0 affects the locations of both the shock wave and the discontinuous derivative at the rightmost characteristic of the rarefaction fan at $t = 1$. The SSC-SR method tracks the discontinuity and the discontinuous derivative using the location of the fronts labeled as the shock wave and the rightmost characteristic by the front tracking method in the physical space. If the discontinuous derivative is difficult to identify, for

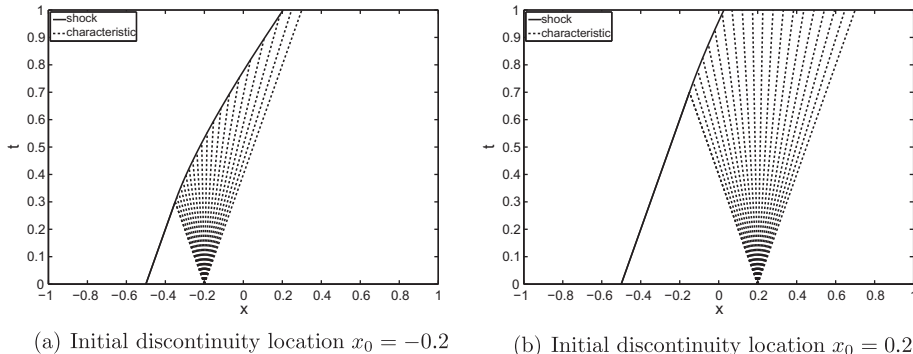


Fig. 19. Front tracking solution in space–time with $u_0 = 1.5$ and $n_f = 20$ characteristics discretizing the rarefaction wave for the inviscid Burgers' equation.

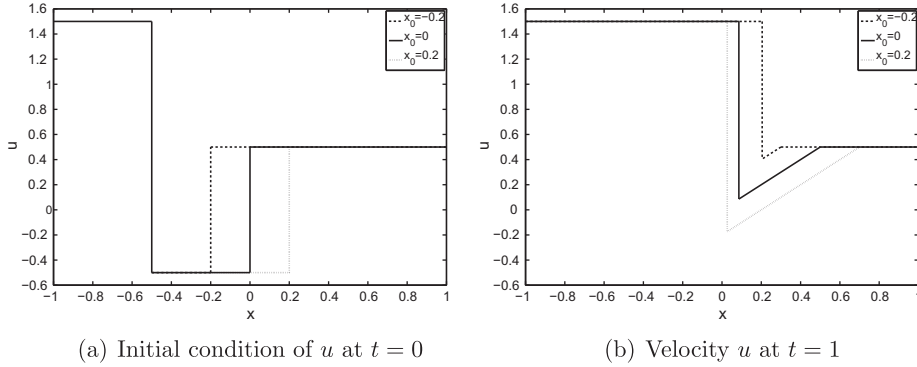


Fig. 20. Velocity u for the initial discontinuity locations $x_0 = \{-0.2, 0, 0.2\}$ with $u_0 = 1.5$ and $n_f = 100$ for the inviscid Burgers' equation.

instance in FVM solutions with numerical diffusion, then it does not need to be modeled explicitly by the SSC-SR method resulting locally in the same solution as SSC-ENO.

The mean $\mu_u(x)$ and the standard deviation $\sigma_u(x)$ of u are given in Figs. 21 and 22 for the random initial discontinuity location x_0 and the deterministic initial value of $u_0 = 1.5$. The results for SSC-ENO and SSC-SR are obtained using $n_s = \{3, 5, 33\}$ and $n_s = \{3, 5, 9\}$ samples, respectively. The steps in the SSC-ENO approximation in the shock region are not equidistant in this case, because of the nonlinearity of the shock path. SSC-SR leads to a more accurate solution for both the shock wave and the discontinuous derivative at the rightmost characteristic. The SSC-SR result further improves in the shock region with an increase of the number of samples from $n_s = 3$ to $n_s = 5$. This is partly caused by the nonlinearity of the response surface for the shock location x_{shock} , shown in Fig. 23(a), which is not fully captured by the quadratic approximation for $n_s = 3$. The effect of the sampling strategy (6) on the location of the samples can be seen for $n_s = 9$ in terms of the concentration of the sampling points near the boundaries of the parameter domain. An example is given below that illustrates the benefits of this non-uniform sampling. Fig. 23(b) shows that the location of the rightmost characteristic x_{char} depends linearly on the random initial discontinuity location x_0 .

An example of the convergence for the discontinuous response surface of u at $x = 0.1$ is given in Fig. 24 for SSC-ENO and SSC-SR with $n_s = \{3, 5, 9\}$. In Fig. 24(b) for SSC-SR, the nonlinearity of the shock path leads to a slightly different discontinuity location for $n_s = 3$ than for the higher values of n_s , which agree with the MC solution. The error convergence is given in Tables 3 and 4 for the mean, standard deviation, and the root mean square (RMS) error ε_{rms} defined by [35]

$$\varepsilon_{\text{rms}} = \sqrt{\frac{1}{n_{\text{mc}}} \sum_{k=1}^{n_{\text{mc}}} (w(\xi_{\text{mc}_k}) - u(\xi_{\text{mc}_k}))^2}, \quad (14)$$

with n_{mc} the number of MC integration points, ξ_{mc_k} , introduced in Appendix A. The given order of convergence \mathcal{O} for SSC-ENO is obtained from the least squares fit through the errors up to $n_s = 33$ samples. SSC-ENO results approximately in first-order convergence for the statistical moments due to the linear approximation in the discontinuous cell. The order of the RMS error ε_{rms} is approximately half of that because of the discontinuity in the response function. SSC-SR shows a faster convergence than SSC-ENO to a smaller error at a lower sample size of $n_s = 9$. The order of convergence is not computed for SSC-SR, because the method is not expected to have a polynomial convergence owing to the simultaneous increase of the number of

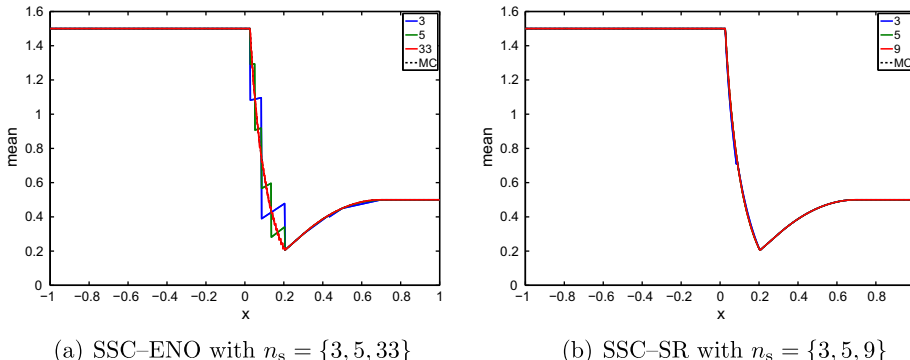


Fig. 21. Mean $\mu_u(x)$ of velocity u for the inviscid Burgers' equation with the random initial discontinuity location x_0 .

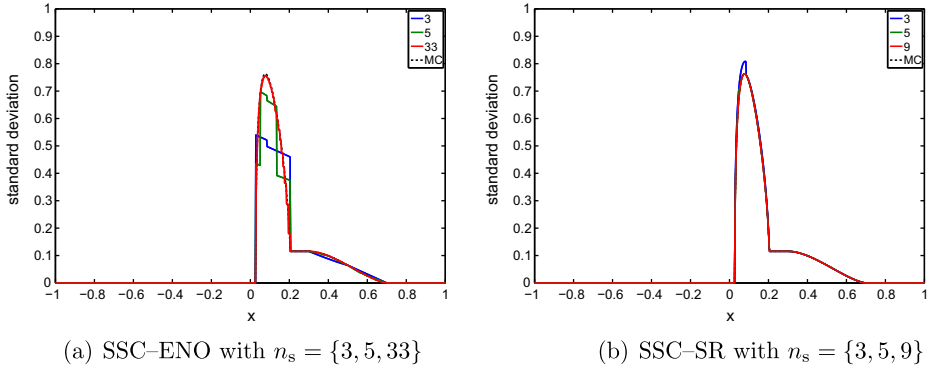


Fig. 22. Standard deviation $\sigma_u(x)$ of velocity u for the inviscid Burgers' equation with the random initial discontinuity location x_0 .

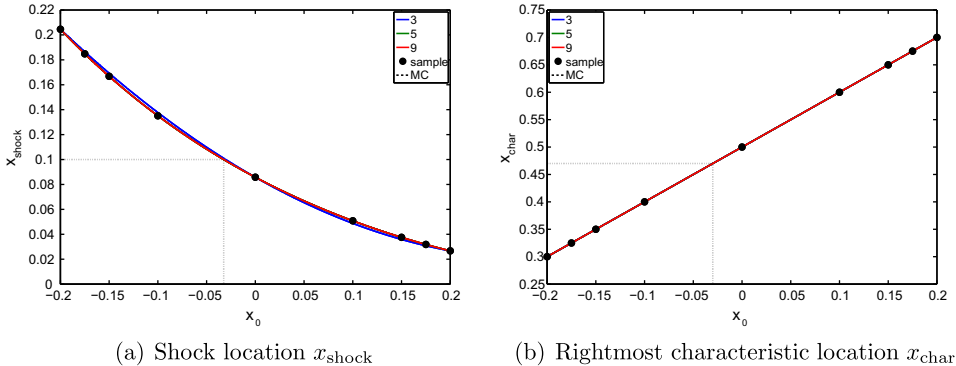


Fig. 23. Response surface approximations for the location of the discontinuity, x_{shock} , and the discontinuous derivative, x_{char} , for the inviscid Burgers' equation with the random initial discontinuity location x_0 .

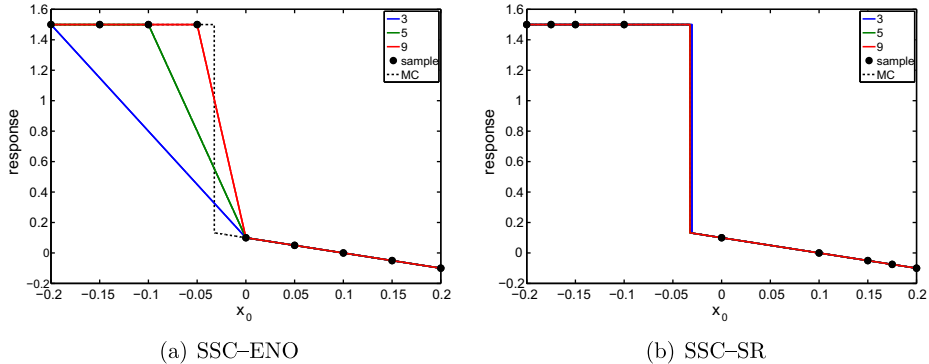


Fig. 24. Response surface approximations for u at $x = 0.1$ with $n_s = \{3, 5, 9\}$ for the inviscid Burgers' equation with the random initial discontinuity location x_0 .

samples and the polynomial interpolation degree. The error obtained with MC using the same number of samples is shown for comparison in Table 5 together with the reference solution for $n_{mc} = 5 \cdot 10^4$. MC is approximately as accurate as SSC-ENO in this case, because of the linear approximation of the discontinuity. SSC-SR results in an error that is also two orders of magnitude smaller than MC, which illustrates the usefulness of the present method.

A response surface for u with a discontinuous derivative is obtained for the x -location of $x = 0.47$ as shown in Fig. 25 for SSC-ENO and SSC-SR with $n_s = \{3, 5, 9\}$. The SSC-SR method obtains the exact solution for $n_s = 3$ because of the correct representation of the discontinuous derivative. Two other cases of SSC-SR response surface approximations are illustrated in Fig. 26 for $x = 0.036$ and $x = 0.66$ with $n_s = \{3, 5, 9\}$. At $x = 0.036$ in Fig. 26(a), the discontinuity in the response surface is located close to the maximum value of the random parameter $x_0 = 0.2$. This leads to a constant approximation to the right

Table 3

Error convergence and order \mathcal{O} for SSC-ENO at $x = 0.1$ for the inviscid Burgers' equation with the random initial discontinuity location x_0 .

n_s	Mean μ_u		Standard deviation σ_u		RMS norm
	Value	Error	Value	Error	ε_{rms}
3	$4.000 \cdot 10^{-1}$	$2.378 \cdot 10^{-1}$	$4.933 \cdot 10^{-1}$	$2.406 \cdot 10^{-1}$	$4.394 \cdot 10^{-1}$
5	$5.750 \cdot 10^{-1}$	$6.276 \cdot 10^{-2}$	$6.591 \cdot 10^{-1}$	$7.477 \cdot 10^{-2}$	$2.349 \cdot 10^{-1}$
9	$6.625 \cdot 10^{-1}$	$2.474 \cdot 10^{-2}$	$7.120 \cdot 10^{-1}$	$2.186 \cdot 10^{-2}$	$1.558 \cdot 10^{-1}$
17	$6.203 \cdot 10^{-1}$	$1.745 \cdot 10^{-2}$	$7.159 \cdot 10^{-1}$	$1.793 \cdot 10^{-2}$	$1.210 \cdot 10^{-1}$
33	$6.418 \cdot 10^{-1}$	$4.035 \cdot 10^{-3}$	$7.281 \cdot 10^{-1}$	$5.717 \cdot 10^{-3}$	$7.340 \cdot 10^{-2}$
\mathcal{O}	–	1.559	–	1.467	0.700

Table 4

Error convergence for SSC-SR at $x = 0.1$ for the inviscid Burgers' equation with the random initial discontinuity location x_0 .

n_{mc}	Mean μ_u		Standard deviation σ_u		RMS norm
	Value	Error	Value	Error	ε_{rms}
3	$6.447 \cdot 10^{-1}$	$6.925 \cdot 10^{-3}$	$7.355 \cdot 10^{-1}$	$1.645 \cdot 10^{-3}$	$9.735 \cdot 10^{-2}$
5	$6.376 \cdot 10^{-1}$	$1.915 \cdot 10^{-4}$	$7.338 \cdot 10^{-1}$	$4.659 \cdot 10^{-5}$	$1.618 \cdot 10^{-2}$
9	$6.377 \cdot 10^{-1}$	$5.470 \cdot 10^{-5}$	$7.338 \cdot 10^{-1}$	$1.330 \cdot 10^{-5}$	$8.649 \cdot 10^{-3}$

Table 5

Error convergence for MC compared to the reference solution at $x = 0.1$ for the inviscid Burgers' equation with the random initial discontinuity location x_0 .

n_s	Mean μ_u		Standard deviation σ_u		ε_{rms}
	Value	Error	Value	Error	
3	$5.222 \cdot 10^{-1}$	$1.155 \cdot 10^{-1}$	$6.935 \cdot 10^{-1}$	$4.032 \cdot 10^{-2}$	–
5	$6.120 \cdot 10^{-1}$	$2.576 \cdot 10^{-2}$	$7.268 \cdot 10^{-1}$	$7.036 \cdot 10^{-3}$	–
9	$6.728 \cdot 10^{-1}$	$3.508 \cdot 10^{-2}$	$7.413 \cdot 10^{-1}$	$7.468 \cdot 10^{-3}$	–
17	$6.280 \cdot 10^{-1}$	$9.735 \cdot 10^{-3}$	$7.314 \cdot 10^{-1}$	$2.465 \cdot 10^{-3}$	–
33	$6.451 \cdot 10^{-1}$	$7.324 \cdot 10^{-3}$	$7.356 \cdot 10^{-1}$	$1.731 \cdot 10^{-3}$	–
$5 \cdot 10^4$	$6.378 \cdot 10^{-1}$	–	$7.338 \cdot 10^{-1}$	–	–

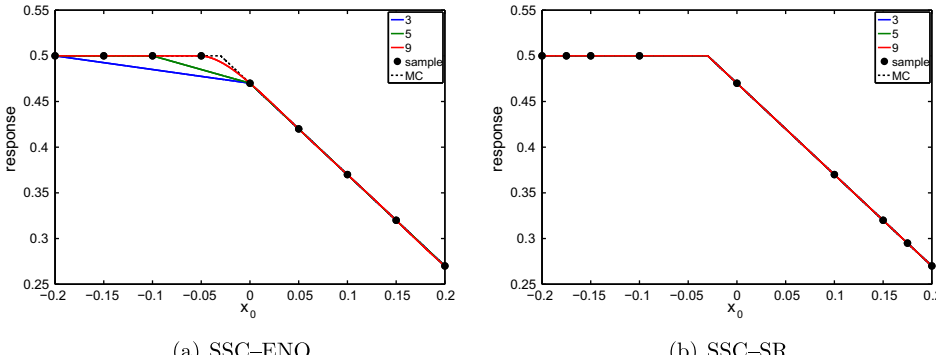


Fig. 25. Response surface approximations for u at $x = 0.47$ with $n_s = \{3, 5, 9\}$ for the inviscid Burgers' equation with the random initial discontinuity x_0 .

of the discontinuity through the only sample at that side of the jump for $n_s = 5$. The sampling strategy (6) focuses on the zeroth order polynomial in this region, such that for $n_s = 9$ a linear approximation is obtained. Fig. 26(b) shows a discontinuous derivative located close to $x_0 = 0.2$ for $x = 0.66$ with only one sampling point at the right of the kink. In that case, the constant approximation near the right boundary for $n_s = \{3, 5\}$ is avoided using the continuity at the location of the discontinuous derivative to construct a linear function at the right of the kink through the rightmost sample.

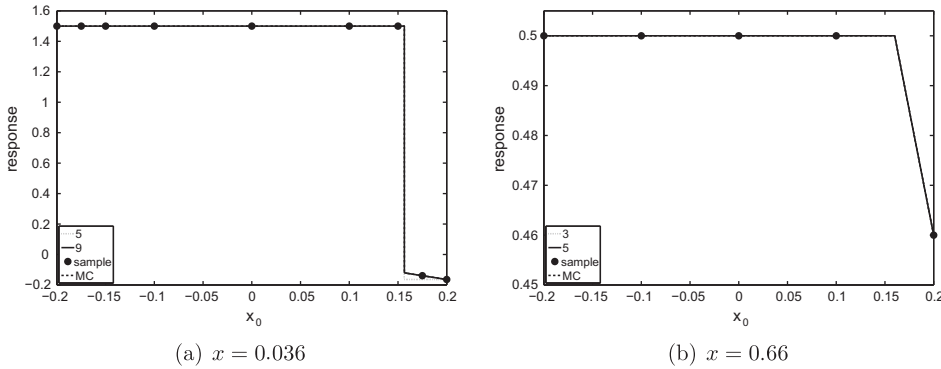


Fig. 26. Response surface approximations of u for SSC-SR with $n_s = \{3, 5, 9\}$ for the inviscid Burgers' equation with the random initial discontinuity location x_0 .

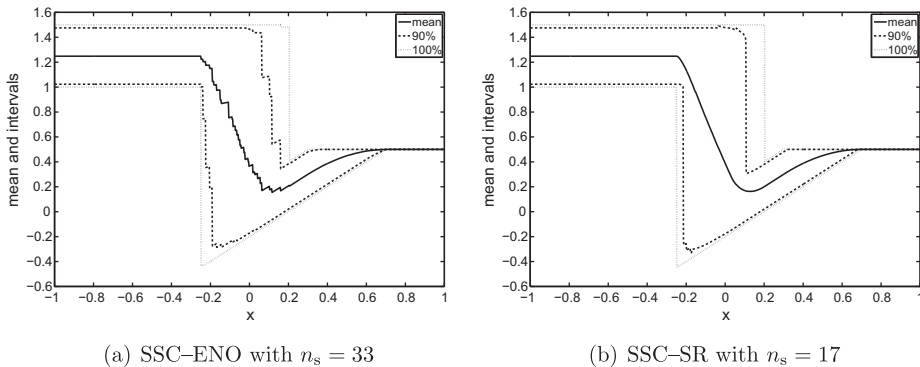


Fig. 27. Mean $\mu_u(x)$, and 90% and 100% probability intervals of u for the inviscid Burgers' equation with the random initial discontinuity location x_0 and initial value u_0 .

4.2. Random initial discontinuity location x_0 and initial value u_0

The effect of the additional randomness in the initial value $u_0 = \mathcal{U}(1; 1.5)$ in (13) is considered next. The resulting variation of the output u between 1 and 1.5 at the left boundary of the spatial domain can be recognized in Fig. 27 for the mean, and 90% and 100% probability intervals of SSC-ENO with $n_s = 33$ and SSC-SR with $n_s = 17$. The size of the intervals shows the varying shock strength in the interaction region caused by the random shock location.

The changing strength of the discontinuity is also visible in the response surface approximations for u in Fig. 28 for the physical location $x = -0.1$. SSC-SR obtains a sharp resolution of both the curvature and the variable strength of the shock in the parameter space compared to the piecewise linear result of SSC-ENO. The curvature is resolved by the nonlinearity of the SSC-SR response surface for the shock location x_{shock} in the physical space as function of x_0 and u_0 shown in Fig. 29(a). The intersection of the piecewise polynomial response surface for x_{shock} with the horizontal plane for $x = -0.1$ gives a higher-degree approximation of the curvature. The response surface for the location of the discontinuous derivative at the rightmost characteristic of the rarefaction fan, x_{char} , is linear in x_0 and independent of u_0 as given in Fig. 29(b). A different axis orientation is used in the latter figure for better visibility.

Examples of response surface approximations by SSC-SR with a discontinuous derivative are given in Fig. 30 for $x = 0.47$ and $x = 0.66$. It shows that the discontinuous derivative has a different orientation in the parameter space than the shock in Fig. 28. These significantly different response surfaces at different x -locations make stochastic problems with random spatial discontinuities challenging to solve. The continuity at the kink in the response surface enables SSC-SR to resolve the discontinuous derivative also when it is located close to the boundary of the parameter space as for $x = 0.66$ in Fig. 30(b).

5. Shock tube problem

Sod's Riemann problem in a closed shock tube is a test case that involves a system of hyperbolic conservation laws, for which the SSC-ENO method has been shown to give a staircase approximation of the discontinuities in [36].

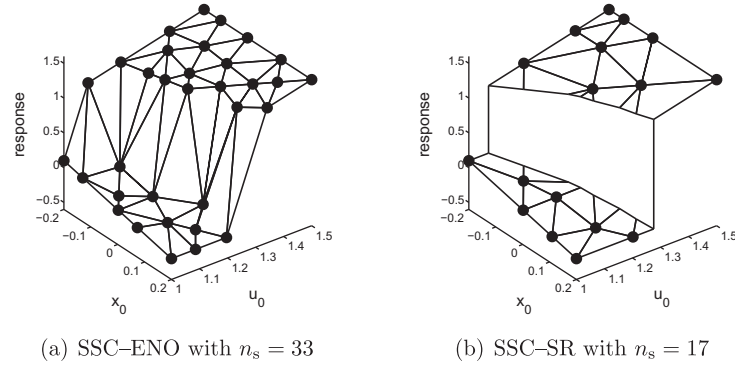


Fig. 28. Response surface approximations for u at $x = -0.1$ as function of the random initial discontinuity location x_0 and initial value u_0 for the inviscid Burgers' equation.

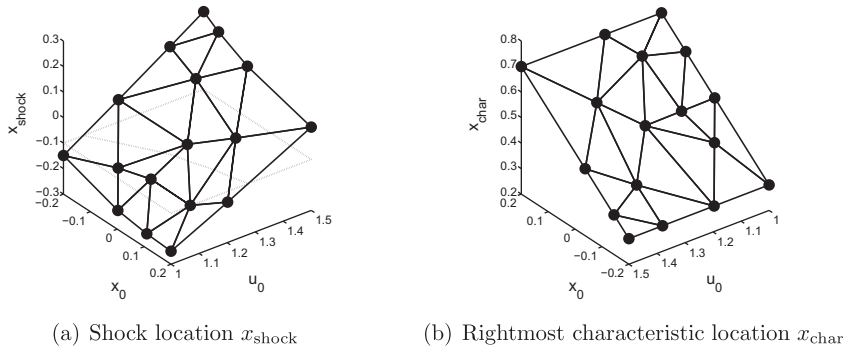


Fig. 29. Response surface approximations as function of the random initial discontinuity location x_0 and initial value u_0 by SSC-SR with $n_s = 17$ for the inviscid Burgers' equation.

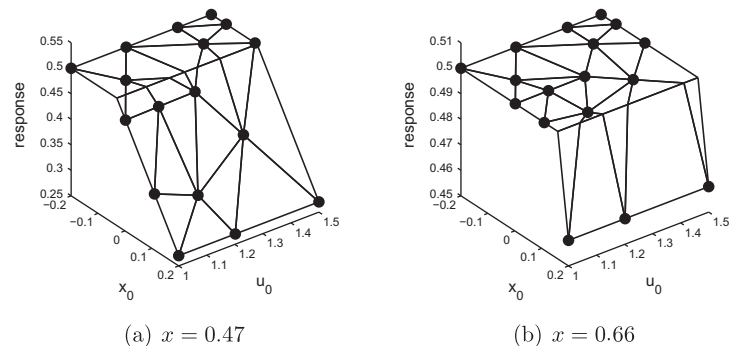


Fig. 30. Response surface approximations for u as function of the random initial discontinuity location x_0 and initial value u_0 by SSC-SR with $n_s = 17$ for the inviscid Burgers' equation.

5.1. Simplex stochastic collocation results

The initial conditions for the static pressure p and the density ρ are given by Sod's Riemann problem on a finite spatial domain $x \in [-0.2; 2]$ with reflecting walls

$$\begin{cases} p_{\text{left}} = 1, & \\ \rho_{\text{left}} = 1, & \end{cases} \quad \begin{cases} p_{\text{right}} = 0.1, & \\ \rho_{\text{right}} = 0.125, & \end{cases} \quad (15)$$

for a fluid at rest with velocity $u = 0$ on both sides of a diaphragm at x_0 . The dynamics of the flow for $t > 0$ is governed by the Euler equations for an inviscid fluid

$$\frac{\partial}{\partial t} \begin{pmatrix} \rho \\ \rho u \\ \rho E \end{pmatrix} + \frac{\partial}{\partial x} \begin{pmatrix} \rho u \\ \rho u^2 + p \\ \rho u H \end{pmatrix} = 0, \quad (16)$$

with $E = (1/(\gamma - 1))p/\rho + u^2/2$, $H = E + p/\rho$, and $\gamma = c_p/c_v$ for the total specific energy E , total specific enthalpy H , the adiabatic coefficient γ , and the specific heats c_p and c_v . The second-order front tracking method is used to solve (16) with $n_f = 64$ fronts discretizing the rarefaction wave. The deterministic solution up to $t = 1$ in Fig. 31(a) shows the interaction of the rarefaction wave with the contact discontinuity. This results in two discontinuities in the density profile in Fig. 31(b) and three points with a discontinuous derivative at $t = 1$, which are tracked by the location of the fronts. The randomness is introduced in the pressure of the initial left state p_{left} and the diaphragm location x_0 given by the uncorrelated uniform distributions $p_{\text{left}} = \mathcal{U}(0.9; 1.1)$ and $x_0 = \mathcal{U}(-0.025; 0.025)$.

The convergence of the mean $\mu_\rho(x)$ and the standard deviation $\sigma_\rho(x)$ of the density ρ at $t = 1$ is shown in Figs. 32 and 33 for SSC-ENO with $n_s = \{10, 20, 100\}$ and SSC-SR with $n_s = \{10, 15, 20\}$. The shock and contact waves are smeared by the random location of the discontinuities in the results for the mean density $\mu_\rho(x)$ with respect to the deterministic solution of Fig. 31(b). The standard deviation $\sigma_\rho(x)$ also has local maxima in the regions of the discontinuity displacement. The results for SSC-SR are indistinguishable and converged to a maximum standard deviation of $\sigma_{\rho,\text{max}} = 0.0730$ at $x = 1.754$ for $n_s = 15$. SSC-ENO underestimates the maximum output randomness with $\sigma_{\rho,\text{max}} = 0.0700$ by 4.16% even for $n_s = 100$.

The 90% and 100% probability intervals are compared to the mean density profile in Fig. 34(a) for SSC-SR with $n_s = 15$. The wide and asymmetrical intervals in the discontinuous regions show the high nonlinearity of the stochastic problem and the randomness in the discontinuity locations. Fig. 34(b) gives the discontinuous SSC-SR response surface approximation of ρ at $x = 0.82$ for $n_s = 15$.

5.2. Comparison with other stochastic methods and spatial discretizations

The overall accuracy of the method depends on the noise in the shock sensor, the convergence of the response surfaces for the discontinuity locations, and the computation of the statistics. In this section, the results are compared to different uncertainty quantification methods for different spatial discretizations to understand whether the sequence of the two stochastic interpolation problems in SSC-SR is robust. The SSC-SR and SSC-ENO results are compared with the following well-established non-intrusive techniques: Monte Carlo (MC) simulation, Polynomial Chaos (PC), and Stochastic Collocation (SC). For a fair comparison between methods, this is done for the following two different numerical methods for the spatial discretization: the Front Tracking Method (FTM) and the Finite Volume Method (FVM). Two different spatial meshes are also used in FVM to demonstrate the effect on the efficiency of SSC-SR and to estimate the influence on the SSC-SR performance. In this way, it can be discussed what level of spatial discretization is needed with respect to direct impact of the relative contribution from the deterministic component of the numerical scheme on the overall error budget. The convergence of the standard deviation $\sigma_\rho(x)$ of the density ρ and of the error in the maximum standard deviation $\sigma_{\rho,\text{max}}$ with respect to a converged MC solution are considered for different numbers of samples and for the different spatial discretizations.

The spectral projection method is used in the non-intrusive PC method, in which a number of random samples is projected onto the orthogonal Legendre PC basis polynomials for computing the PC coefficients [25]. A different set of random sampling points is used here to assess the convergence of PC and MC than in the MC reference solution. A first-order polynomial basis is employed for PC in this section, since higher-degree polynomials result in nonphysical negative values for the gas density ρ . Similar results for higher-degree PC are added in Section 5.3. The quality of all the other methods is also

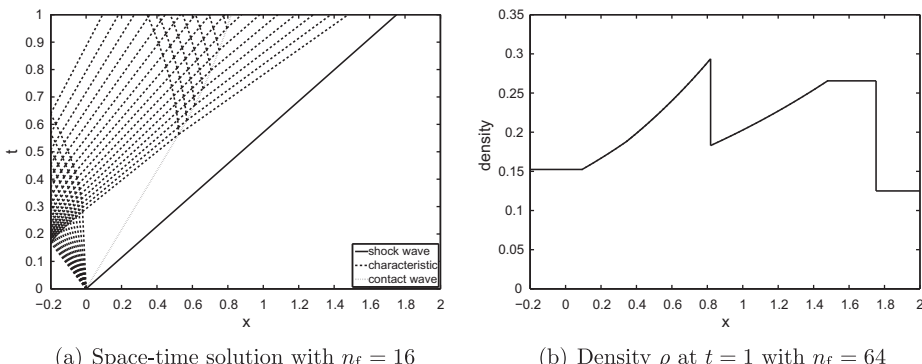


Fig. 31. Sod's Riemann problem in a closed shock tube.

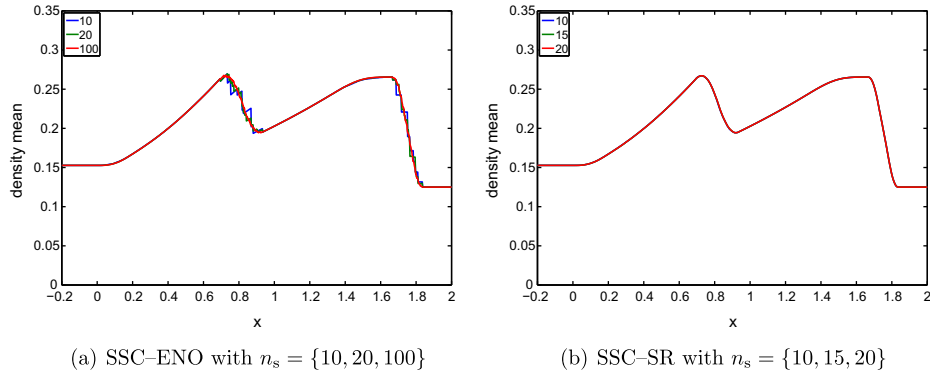


Fig. 32. Mean $\mu_\rho(x)$ of the density ρ for Sod's Riemann problem in a closed shock tube with random initial pressure p_{left} and diaphragm location x_0 .

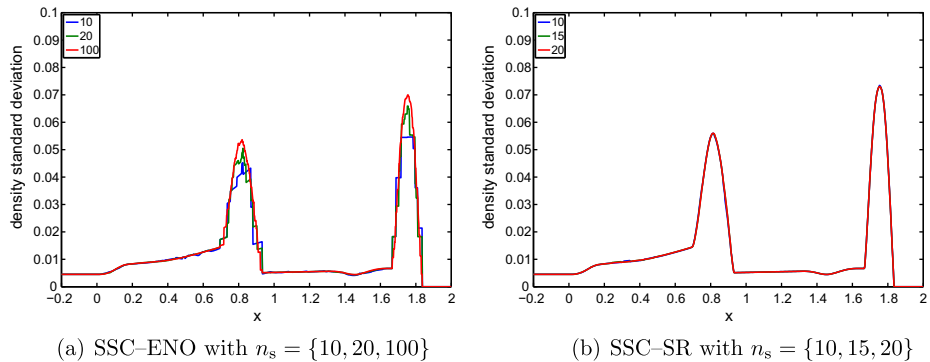


Fig. 33. Standard deviation $\sigma_\rho(x)$ of the density ρ for Sod's Riemann problem in a closed shock tube with random initial pressure p_{left} and diaphragm location x_0 .

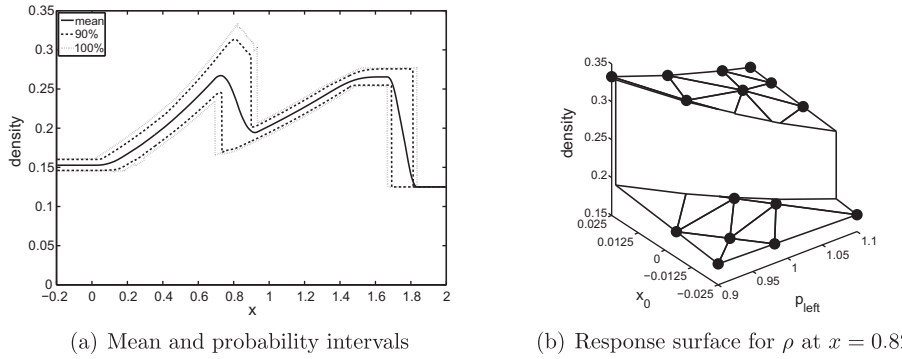


Fig. 34. SSC-SR results with $n_s = 15$ for Sod's Riemann problem in a closed shock tube with random initial pressure p_{left} and diaphragm location x_0 .

considered at this level. The quality of the representation furnished by all the other methods does not lead to nonphysical negative values for the gas density. The SC method is based on hierarchical sampling at the tensor product of Clenshaw-Curtis quadrature points and global Lagrangian polynomial interpolation [38]. The FVM spatial discretization uses a second-order Godonov method with a minmod slope limiter [27] and a CFL number of 0.25 on a coarse mesh of $n_x = 88$ spatial volumes and a fine mesh with $n_x = 352$. These mesh sizes have been selected after a convergence study for the density $\rho(x)$ of the deterministic problem at the nominal inputs. The deterministic solutions on these coarse and fine FVM meshes are shown in Fig. 35 for the nominal initial conditions. The discontinuities are smeared especially in the coarse approximation to see what happens if the fronts are not accurately captured. The uncertain initial conditions are implemented in such a way that the discretized cell averages are equal to the exact initial conditions averaged over the volume. The discontinuity locations are extracted from the FVM solutions as defined in Section 6.

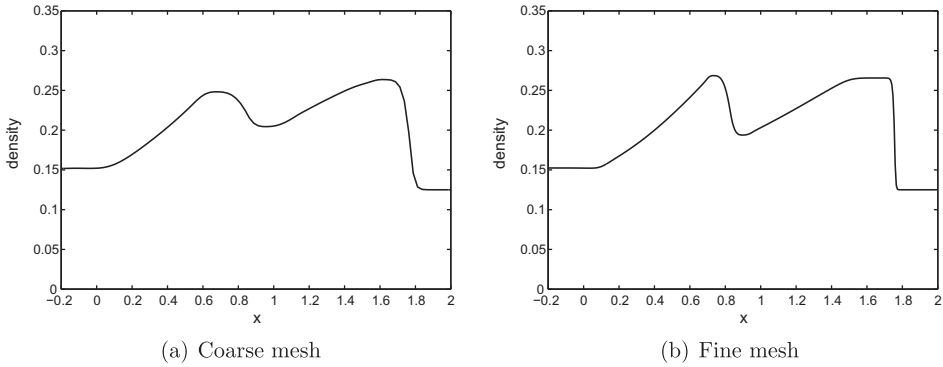


Fig. 35. Deterministic FVM solutions of Sod's Riemann problem in a closed shock tube.

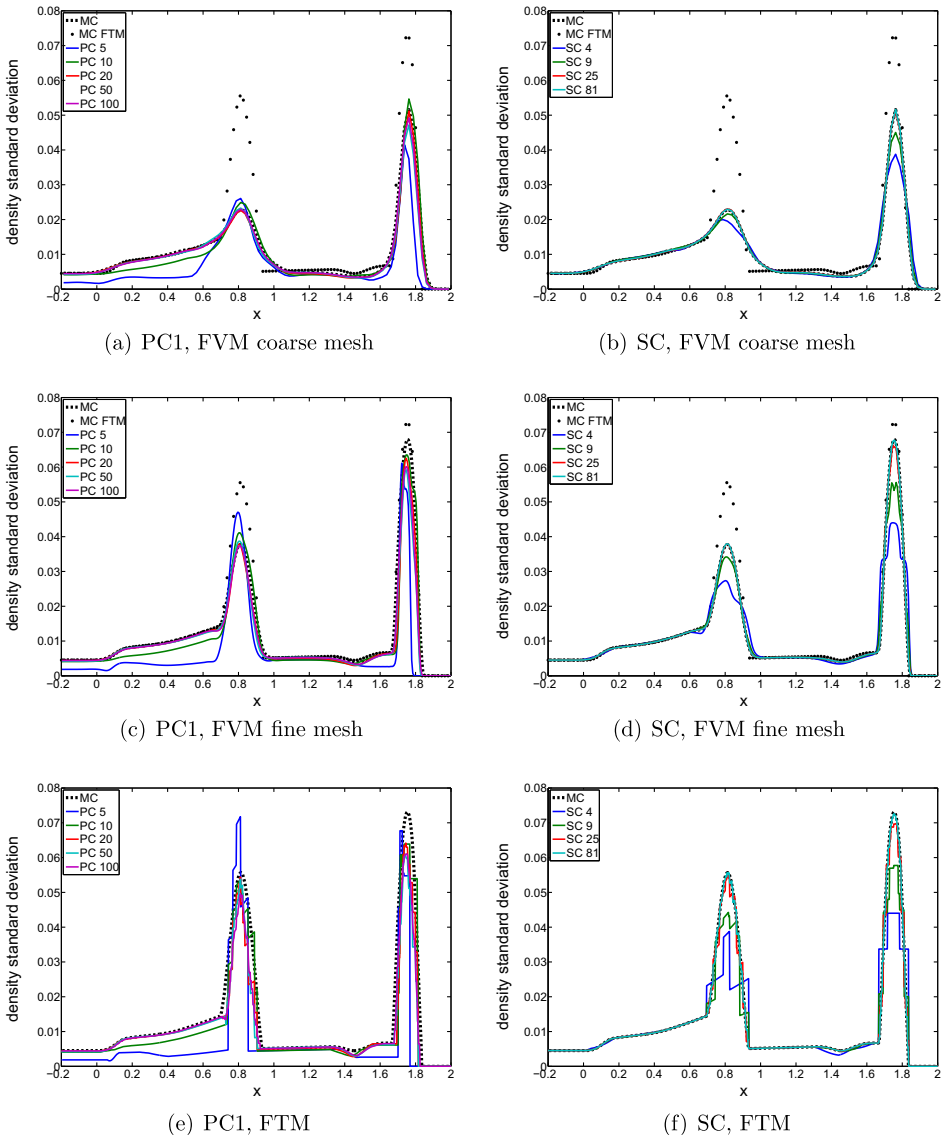


Fig. 36. Standard deviation $\sigma_\rho(x)$ of the density ρ for Sod's Riemann problem in a closed shock tube for the PC1 and SC stochastic methods and the FVM and FTM spatial discretizations.

The numerical results for the standard deviation $\sigma_\rho(x)$ of PC1 and SC are shown in Fig. 36 and of SSC-ENO and SSC-SR in Fig. 37 with $n_s = \{5, 10, 20, 50, 100\}$. The number of samples for SC is $n_s = \{4, 9, 25, 81\}$ because of the limited flexibility of choosing the number of its quadrature points. The set of SC quadrature points is not considered for all the methods to demonstrate the flexibility of choosing the number of points in the other methods. The results are compared to those of the MC reference solutions both from the same spatial mesh and from the FTM spatial discretization. The difference between the MC reference solutions with the FVM and FTM spatial discretizations shows that the numerical diffusion of the discontinuities in FVM results in an underprediction of the standard deviation compared to FTM. The MC-FVM reference solutions converge to those with the FTM discretization for an increasing spatial mesh size. The first-order PC1 method does not converge to the MC reference solutions, because the linear polynomial is insufficient to capture the nonlinear response surface. This error increases with an increasingly accurate spatial solution on the fine mesh and with the inviscid FTM discretization. The SC predictions approach the MC reference solution with the same spatial discretization. The global polynomial of SC converges well for the relatively smooth solution on the coarse FVM mesh. The problem of the staircase solution of the statistics is also not present for the coarse approximation because of the numerical smearing of the discontinuity. However, the accuracy of the SC approximation also decreases with an increasing spatial resolution, especially for smaller sample sizes.

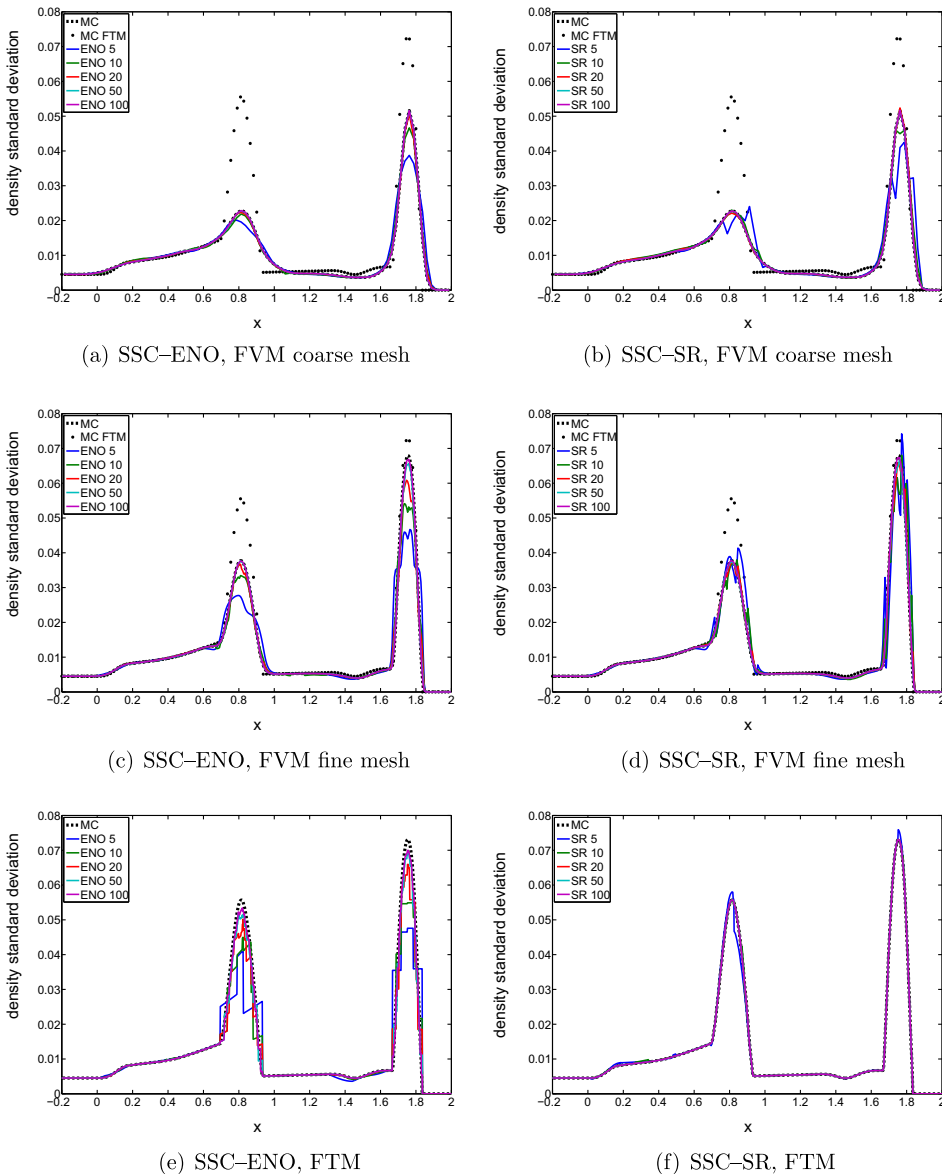


Fig. 37. Standard deviation $\sigma_\rho(x)$ of the density ρ for Sod's Riemann problem in a closed shock tube for the SSC-ENO and SSC-SR stochastic methods and the FVM and FTM spatial discretizations.

Fig. 37 shows that SSC–ENO has a similar convergence behavior and accuracy as the SC method. The rate of convergence of SSC–SR for the coarse FVM discretization is comparable to that of SSC–ENO. In contrast to SC and SSC–ENO, the SSC–SR convergence improves for the more accurate spatial solutions from the fine FVM mesh and the FTM discretization. This is an important desirable property of SSC–SR, since simultaneous convergence in both the physical space and the probability space is usually required.

The error convergence of the maximum standard deviation $\sigma_{\rho_{\max}}$ is given in **Tables 6–12**, where $\sigma_{\rho_{\max}}$ is defined as $\max_{x \in [-0.2; 2]} \sigma_{\rho}(x)$. The results of MC, PC1, SSC–ENO, and SSC–SR for the coarse and fine FVM, and the FTM discretization compared to the reference MC solution for the same discretization are reported in **Tables 6–8**. It confirms that MC has slow convergence and that PC1 does not converge to the reference solution for an increasing number of samples. SSC–SR leads to a smaller error than SSC–ENO for all cases, which illustrates the benefit of the subcell resolution. The equivalent results for the SC method in **Table 9** show that its stochastic accuracy decreases consistently with increasing spatial accuracy for the same number of samples. It can be concluded that SSC–SR is the most accurate method with a decreasing error with increasing spatial resolution for the small sample sizes of $n_s \leq 10$, such that SSC–SR results in high accuracy at low computational costs. This demonstrates that the sequence of the two stochastic problems in SSC–SR is robust enough for this situation. SSC–SR also converges to the lowest error at $n_s = 100$ for both the FTM method and one FVM spatial discretization. The improvement is largest for the most accurate FTM spatial discretization with a reduction of the error by at least four orders of magnitude compared to the other stochastic methods.

Tables 10–12 contain the convergence of $\sigma_{\rho_{\max}}$ on the FVM meshes with respect to the inviscid FTM reference solution. The underestimation of $\sigma_{\rho_{\max}}$ by the MC reference solutions on the coarse and fine FVM meshes gives an error of $2.148 \cdot 10^{-2}$ and $5.169 \cdot 10^{-3}$, respectively, compared to the one for FTM. None of the stochastic methods converges to a value below these reference errors caused by the spatial accuracy, since they converge to the MC solution with the same spatial discretization. Therefore, the results of the stochastic methods for the FTM spatial discretization give the best indication of their convergence to the true solution without underprediction of $\sigma_{\rho_{\max}}$ by numerical diffusion. Also in that respect, the proposed SSC–SR method leads to the highest accuracy for the most relevant case. SSC–SR is compared to more advanced stochastic methods for more complex flow problems in [17].

5.3. Higher-degree PC

In Section 5.2 the PC is limited to first order polynomials due to nonphysical negative values for the gas density prediction for higher-degree polynomials. If one does not consider the quality of the polynomial representation furnished by the PC, the statistics evaluation can be always obtained even for the high-degree polynomials. Similar results are added in this section.

The numerical results for $\sigma_{\rho}(x)$ of PC with higher-order polynomial degrees, $p = 2$ and $p = 3$, are shown in **Fig. 38**. The range of the vertical axis is extended to $\sigma_{\rho}(x) = [0, 0.12]$, because of the large overshoots for PC3 and low numbers of samples in combination with the FTM spatial discretization. It shows that higher polynomial degrees in PC do not improve the solution and the accuracy becomes worse for low sample sizes. The nonphysical predictions contribute to these conclusions for the statistics evaluation.

In **Tables 13–17**, the error convergence of the maximum standard deviation $\sigma_{\rho_{\max}}$ is given. The results confirm that the accuracy does not notably improve with an increasing global polynomial degree in this case due to the discontinuous response.

6. Transonic flow over the RAE 2822 airfoil

Non-uniform probability distributions are considered in a FVM discretization of multiple spatial dimensions for the transonic flow over the RAE 2822 airfoil [11]. The randomness in this NODESIM–CFD test case [21] is given by independent normal distributions for the free-stream Mach number M_∞ and the angle of attack α with the mean values 0.734 and 2.79° , and standard deviations 0.005 and 0.1° , respectively. The flow problem is solved using an upwind discretization of the inviscid Euler equations in FLUENT to obtain a sharp discontinuity in the flow field up to the pressure distribution on the airfoil surface. The deterministic results for the two-dimensional spatial discretization with a structured grid of $5 \cdot 10^4$ cells are shown

Table 6

Error in the maximum standard deviation $\sigma_{\rho_{\max}}$ of the density ρ compared to the MC reference solution of $\sigma_{\rho_{\max}} = 5.161 \cdot 10^{-2}$ with the coarse mesh FVM spatial discretization for Sod's Riemann problem in a closed shock tube.

n_s	MC	PC1	SSC–ENO	SSC–SR
5	$1.420 \cdot 10^{-2}$	$1.011 \cdot 10^{-2}$	$1.288 \cdot 10^{-2}$	$9.075 \cdot 10^{-3}$
10	$3.114 \cdot 10^{-3}$	$3.045 \cdot 10^{-3}$	$4.956 \cdot 10^{-3}$	$5.615 \cdot 10^{-3}$
20	$2.059 \cdot 10^{-3}$	$4.173 \cdot 10^{-4}$	$9.289 \cdot 10^{-4}$	$7.558 \cdot 10^{-4}$
50	$3.428 \cdot 10^{-3}$	$4.420 \cdot 10^{-5}$	$4.124 \cdot 10^{-5}$	$1.625 \cdot 10^{-5}$
100	$7.941 \cdot 10^{-5}$	$2.410 \cdot 10^{-5}$	$2.062 \cdot 10^{-5}$	$6.907 \cdot 10^{-6}$

Table 7

Error in the maximum standard deviation $\sigma_{\rho_{\max}}$ of the density ρ compared to the MC reference solution of $\sigma_{\rho_{\max}} = 6.814 \cdot 10^{-2}$ with the fine mesh FVM spatial discretization for Sod's Riemann problem in a closed shock tube.

n_s	MC	PC1	SSC-ENO	SSC-SR
5	$8.077 \cdot 10^{-3}$	$6.818 \cdot 10^{-3}$	$2.122 \cdot 10^{-2}$	$6.274 \cdot 10^{-3}$
10	$1.542 \cdot 10^{-3}$	$4.415 \cdot 10^{-3}$	$1.378 \cdot 10^{-2}$	$1.240 \cdot 10^{-4}$
20	$2.213 \cdot 10^{-3}$	$5.401 \cdot 10^{-3}$	$7.061 \cdot 10^{-3}$	$2.027 \cdot 10^{-3}$
50	$1.742 \cdot 10^{-3}$	$8.705 \cdot 10^{-3}$	$2.288 \cdot 10^{-3}$	$1.304 \cdot 10^{-3}$
100	$1.747 \cdot 10^{-4}$	$7.752 \cdot 10^{-3}$	$1.078 \cdot 10^{-3}$	$5.610 \cdot 10^{-4}$

Table 8

Error in the maximum standard deviation $\sigma_{\rho_{\max}}$ of the density ρ compared to the MC reference solution of $\sigma_{\rho_{\max}} = 7.309 \cdot 10^{-2}$ with the FTM spatial discretization for Sod's Riemann problem in a closed shock tube.

n_s	MC	PC1	SSC-ENO	SSC-SR
5	$4.542 \cdot 10^{-3}$	$1.328 \cdot 10^{-3}$	$2.551 \cdot 10^{-2}$	$2.814 \cdot 10^{-3}$
10	$1.740 \cdot 10^{-3}$	$9.203 \cdot 10^{-3}$	$1.819 \cdot 10^{-2}$	$2.003 \cdot 10^{-5}$
20	$1.074 \cdot 10^{-3}$	$8.912 \cdot 10^{-3}$	$7.160 \cdot 10^{-3}$	$1.952 \cdot 10^{-7}$
50	$1.200 \cdot 10^{-3}$	$1.267 \cdot 10^{-2}$	$3.842 \cdot 10^{-3}$	$8.003 \cdot 10^{-7}$
100	$5.176 \cdot 10^{-4}$	$1.207 \cdot 10^{-2}$	$3.101 \cdot 10^{-3}$	$3.137 \cdot 10^{-8}$

Table 9

Error in the maximum standard deviation $\sigma_{\rho_{\max}}$ of the density ρ for the SC stochastic method compared to the MC reference solutions for Sod's Riemann problem in a closed shock tube.

n_s	FVM coarse mesh	FVM fine mesh	FTM
4	$1.284 \cdot 10^{-2}$	$2.393 \cdot 10^{-2}$	$2.909 \cdot 10^{-2}$
9	$6.569 \cdot 10^{-3}$	$1.234 \cdot 10^{-2}$	$1.535 \cdot 10^{-2}$
25	$3.962 \cdot 10^{-4}$	$1.556 \cdot 10^{-3}$	$3.208 \cdot 10^{-3}$
81	$2.699 \cdot 10^{-5}$	$2.062 \cdot 10^{-4}$	$4.649 \cdot 10^{-4}$

Table 10

Error in the maximum standard deviation $\sigma_{\rho_{\max}}$ of the density ρ for the coarse mesh FVM spatial discretization compared to the MC reference solution with the FTM spatial discretization for Sod's Riemann problem in a closed shock tube.

n_s	MC	PC1	SSC-ENO	SSC-SR
5	$3.568 \cdot 10^{-2}$	$3.158 \cdot 10^{-2}$	$3.436 \cdot 10^{-2}$	$3.055 \cdot 10^{-2}$
10	$1.836 \cdot 10^{-2}$	$1.843 \cdot 10^{-2}$	$2.643 \cdot 10^{-2}$	$2.709 \cdot 10^{-2}$
20	$2.354 \cdot 10^{-2}$	$2.189 \cdot 10^{-2}$	$2.241 \cdot 10^{-2}$	$2.072 \cdot 10^{-2}$
50	$2.490 \cdot 10^{-2}$	$2.590 \cdot 10^{-2}$	$2.152 \cdot 10^{-2}$	$2.149 \cdot 10^{-2}$
100	$2.140 \cdot 10^{-2}$	$2.389 \cdot 10^{-2}$	$2.150 \cdot 10^{-2}$	$2.147 \cdot 10^{-2}$

Table 11

Error in the maximum standard deviation $\sigma_{\rho_{\max}}$ of the density ρ for the fine mesh FVM spatial discretization compared to the MC reference solution with the FTM spatial discretization for Sod's Riemann problem in a closed shock tube.

n_s	MC	PC1	SSC-ENO	SSC-SR
5	$1.325 \cdot 10^{-2}$	$1.199 \cdot 10^{-2}$	$2.639 \cdot 10^{-2}$	$1.105 \cdot 10^{-3}$
10	$6.712 \cdot 10^{-3}$	$9.584 \cdot 10^{-3}$	$1.895 \cdot 10^{-2}$	$5.045 \cdot 10^{-3}$
20	$7.382 \cdot 10^{-3}$	$1.057 \cdot 10^{-2}$	$1.223 \cdot 10^{-2}$	$7.196 \cdot 10^{-3}$
50	$6.911 \cdot 10^{-3}$	$1.387 \cdot 10^{-2}$	$7.457 \cdot 10^{-3}$	$6.473 \cdot 10^{-3}$
100	$4.994 \cdot 10^{-3}$	$1.292 \cdot 10^{-2}$	$6.247 \cdot 10^{-3}$	$5.730 \cdot 10^{-3}$

in Fig. 39 in terms of the static pressure field around the airfoil and the distribution of the pressure coefficient C_p over the surface

$$C_p = \frac{p - p_\infty}{\frac{1}{2} \rho_\infty u_\infty^2}, \quad (17)$$

Table 12

Error in the maximum standard deviation $\sigma_{\rho_{\max}}$ of the density ρ for the SC stochastic method compared to the MC reference solution with the FTM spatial discretization for Sod's Riemann problem in a closed shock tube.

n_s	FVM coarse mesh	FVM fine mesh
4	$3.432 \cdot 10^{-2}$	$2.909 \cdot 10^{-2}$
9	$2.805 \cdot 10^{-2}$	$1.750 \cdot 10^{-2}$
25	$2.187 \cdot 10^{-2}$	$6.725 \cdot 10^{-3}$
81	$2.145 \cdot 10^{-2}$	$5.375 \cdot 10^{-3}$

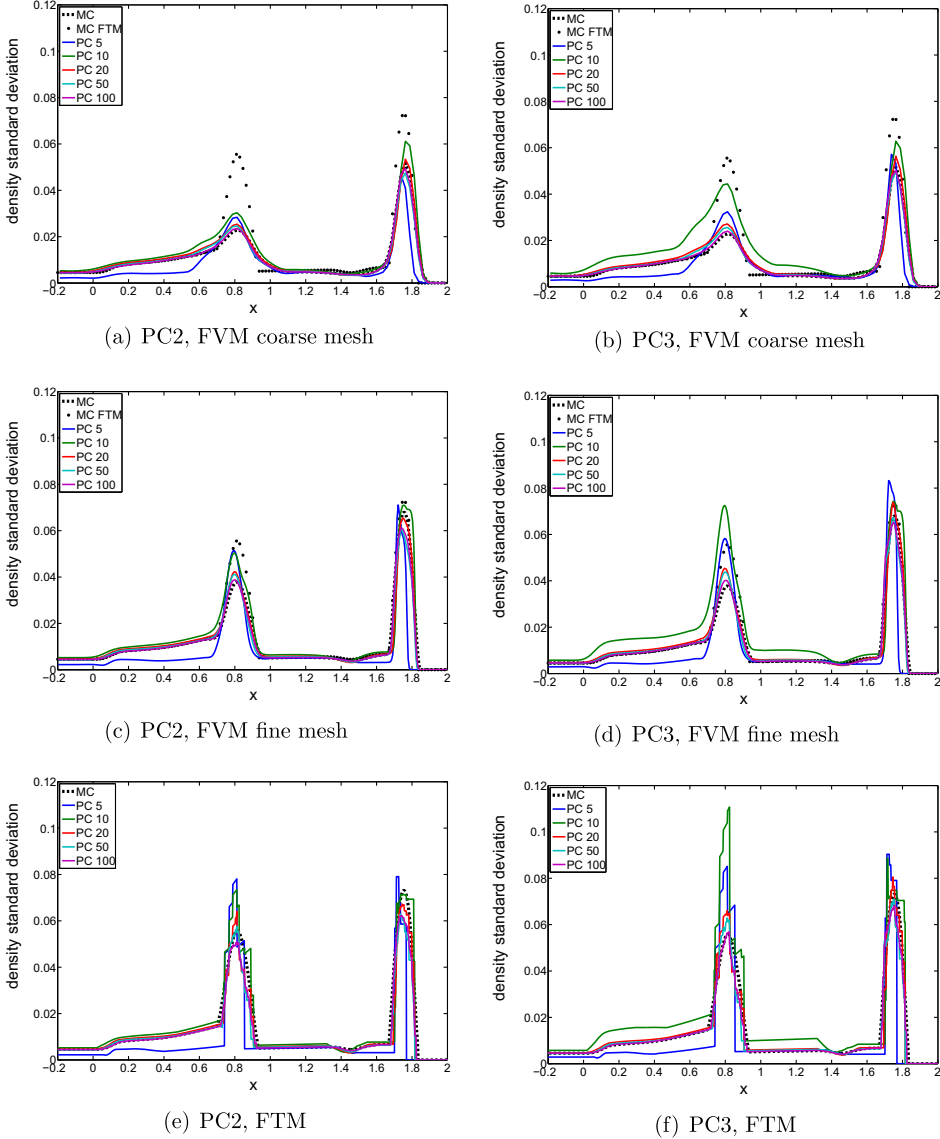


Fig. 38. Standard deviation $\sigma_{\rho}(x)$ of the density ρ for Sod's Riemann problem in a closed shock tube for the higher-degree PC stochastic method and the FVM and FTM spatial discretizations.

where the subscript ∞ denotes the free-stream conditions of the pressure, the density, and the velocity. A transonic shock wave forms above the airfoil, which results in a discontinuity in the surface pressure distribution. The undershoot downstream of the shock wave is caused by the expansion present after an inviscid shock in a transonic flow. An image showing the mesh in the proximity of the airfoil and in the region of the shock is shown in Fig. 40. The mesh size is chosen based on a convergence study for this pressure coefficient profile of the deterministic problem for the nominal boundary conditions.

Table 13

Error for the higher-degree PC stochastic method in the maximum standard deviation $\sigma_{\rho_{\max}}$ of the density ρ compared to the MC reference solution of $\sigma_{\rho_{\max}} = 5.161 \cdot 10^{-2}$ with the coarse mesh FVM spatial discretization for Sod's Riemann problem in a closed shock tube.

n_s	PC2	PC3
5	$4.968 \cdot 10^{-3}$	$5.581 \cdot 10^{-3}$
10	$9.526 \cdot 10^{-3}$	$1.122 \cdot 10^{-2}$
20	$1.791 \cdot 10^{-3}$	$4.695 \cdot 10^{-3}$
50	$4.171 \cdot 10^{-3}$	$1.776 \cdot 10^{-3}$
100	$2.223 \cdot 10^{-3}$	$1.417 \cdot 10^{-3}$

Table 14

Error for the higher-degree PC stochastic method in the maximum standard deviation $\sigma_{\rho_{\max}}$ of the density ρ compared to the MC reference solution of $\sigma_{\rho_{\max}} = 6.814 \cdot 10^{-2}$ with the fine mesh FVM spatial discretization for Sod's Riemann problem in a closed shock tube.

n_s	PC2	PC3
5	$3.177 \cdot 10^{-3}$	$1.534 \cdot 10^{-2}$
10	$3.094 \cdot 10^{-3}$	$6.328 \cdot 10^{-3}$
20	$2.566 \cdot 10^{-3}$	$5.926 \cdot 10^{-3}$
50	$7.439 \cdot 10^{-3}$	$5.986 \cdot 10^{-4}$
100	$6.813 \cdot 10^{-3}$	$2.776 \cdot 10^{-3}$

Table 15

Error for the higher-degree PC stochastic method in the maximum standard deviation $\sigma_{\rho_{\max}}$ of the density ρ compared to the MC reference solution of $\sigma_{\rho_{\max}} = 7.309 \cdot 10^{-2}$ with the FTM spatial discretization for Sod's Riemann problem in a closed shock tube.

n_s	PC2	PC3
5	$5.972 \cdot 10^{-3}$	$1.727 \cdot 10^{-2}$
10	$3.562 \cdot 10^{-4}$	$3.764 \cdot 10^{-2}$
20	$5.909 \cdot 10^{-3}$	$7.463 \cdot 10^{-3}$
50	$1.016 \cdot 10^{-2}$	$2.155 \cdot 10^{-3}$
100	$1.087 \cdot 10^{-2}$	$4.781 \cdot 10^{-3}$

Table 16

Error for the higher-degree PC stochastic method in the maximum standard deviation $\sigma_{\rho_{\max}}$ of the density ρ for the coarse mesh FVM spatial discretization compared to the MC reference solution with the FTM spatial discretization for Sod's Riemann problem in a closed shock tube.

n_s	PC2	PC3
5	$2.645 \cdot 10^{-2}$	$1.590 \cdot 10^{-2}$
10	$1.195 \cdot 10^{-2}$	$1.026 \cdot 10^{-2}$
20	$1.969 \cdot 10^{-2}$	$1.678 \cdot 10^{-2}$
50	$2.565 \cdot 10^{-2}$	$2.325 \cdot 10^{-2}$
100	$2.370 \cdot 10^{-2}$	$2.289 \cdot 10^{-2}$

Table 17

Error for the higher-degree PC stochastic method in the maximum standard deviation $\sigma_{\rho_{\max}}$ of the density ρ for the fine mesh FVM spatial discretization compared to the MC reference solution with the FTM spatial discretization for Sod's Riemann problem in a closed shock tube.

n_s	PC2	PC3
5	$1.992 \cdot 10^{-3}$	$1.017 \cdot 10^{-2}$
10	$2.075 \cdot 10^{-3}$	$1.159 \cdot 10^{-3}$
20	$7.736 \cdot 10^{-3}$	$7.570 \cdot 10^{-4}$
50	$1.261 \cdot 10^{-2}$	$5.768 \cdot 10^{-3}$
100	$1.198 \cdot 10^{-2}$	$7.945 \cdot 10^{-3}$

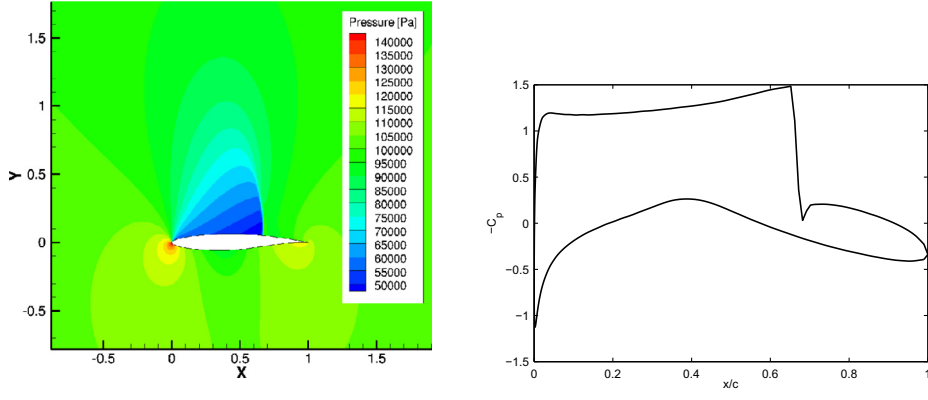


Fig. 39. Deterministic results for the transonic flow over the RAE 2822 airfoil.

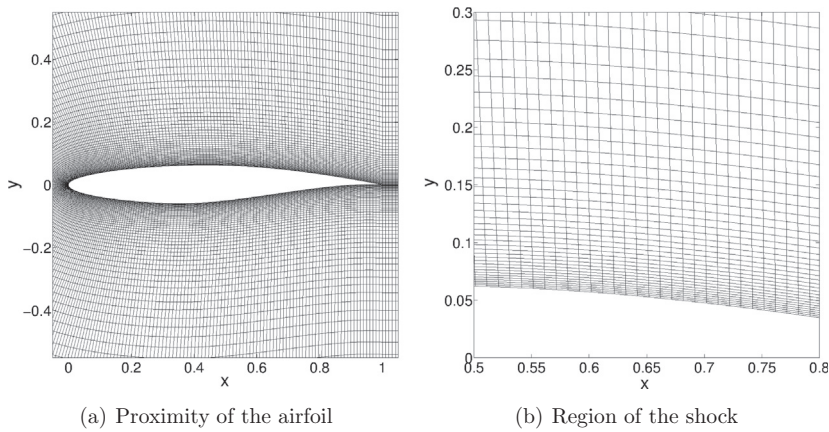


Fig. 40. Spatial Euler mesh for the transonic flow over the RAE 2822 airfoil.

6.1. Simplex stochastic collocation results

The shock location x_{shock} along the airfoil is parameterized by SSC-SR for resolving the stochastic surface pressure distribution. The shock sensor of Harten [13] is used to extract x_{shock} from each of the samples, based on the maximum of the gradient magnitude of the pressure coefficient $|dC_p/dx|$ in the shock region. A discrete resolution of the shock location, limited to the spatial cell faces, is avoided by defining x_{shock} as the extremum of a parabolic fit through the maximum of $|dC_p/dx|$ and

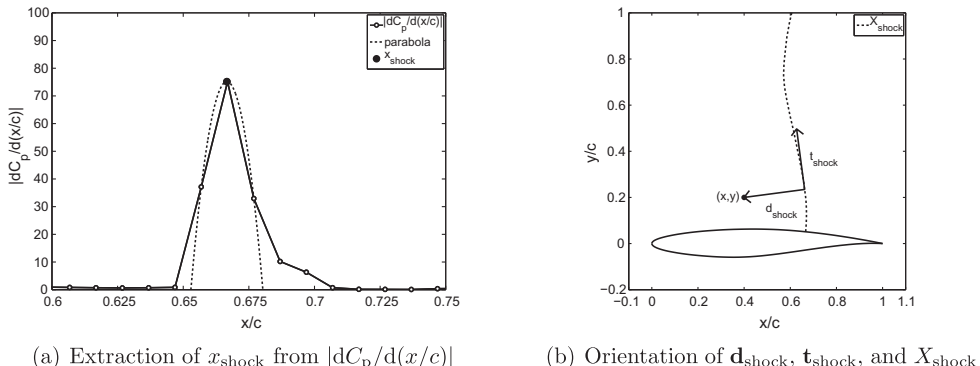


Fig. 41. The SSC-SR algorithm for the transonic flow over the RAE 2822 airfoil at the nominal flow conditions.

the values at its two neighboring spatial points. This approach is illustrated for the nominal flow conditions in Fig. 41(a), for which a shock location of $x_{\text{shock}} = 0.667$ is found.

The extraction step \mathcal{E} is repeated on each layer of cells above the airfoil to obtain the two-dimensional shape of the shock wave X_{shock} for resolving the stochastic pressure field. In that case, the signed distance d_{shock} between the points in the spatial mesh (x, y) and the closest point on the shock wave is parameterized instead of the shock location x_{shock} . The sign of d_{shock} is obtained from the cross product $\mathbf{d}_{\text{shock}} \times \mathbf{t}_{\text{shock}}$ between the vector $\mathbf{d}_{\text{shock}}$ from the point on the shock to the spatial point (x, y) and the tangent vector $\mathbf{t}_{\text{shock}}$ on the shock wave, with $d_{\text{shock}} = \|\mathbf{d}_{\text{shock}}\|$. To that end, the third component of the vector $\mathbf{d}_{\text{shock}} \times \mathbf{t}_{\text{shock}}$ is considered, since it changes sign when the reference point (x, y) crosses the shock wave X_{shock} . The orientation of the vectors $\mathbf{d}_{\text{shock}}$ and $\mathbf{t}_{\text{shock}}$ with respect to the shock X_{shock} is shown in Fig. 41(b) for the nominal flow conditions. An alternative for three spatial dimensions is to define the sign of d_{shock} by whether the point (x, y) is located upstream or downstream of the shock X_{shock} . It needs to be ensured that the shock representation on unstructured grids is good enough to allow this technique, see for example the shock sensors for unstructured grids in [24]. The unbounded range of the normal distribution is treated by truncating the probability space beyond the last MC integration point used for calculating the statistical moments as in [35]. The probabilistic weighting by the normal distribution is accounted for by the sampling strategy (6).

The mean of the pressure coefficient $\mu_{C_p}(x)$ along the airfoil is given in Fig. 42 as function of the x coordinate normalized by the chord length c for SSC-ENO and SSC-SR with $n_s = \{5, 17, 50\}$. The steps in the staircase approximation of SSC-ENO have different strengths in this case due to the non-uniform distribution of the probability over the parameter space. The SSC-ENO solution smoothens for an increasing number of samples, partly because of the presence of numerical diffusion in FVM for solving the Euler equations. However, SSC-ENO overestimates the length of the region over which the shock wave is smeared in the mean pressure distribution compared to the SSC-SR results, which show good convergence already for $n_s = 5$. The minor oscillations in both results are caused by the physical undershoot downstream of the shock in the deterministic solution shown in Fig. 39(b). The effect of this local post-shock expansion in the samples on the statistics converges with an increasing number of samples.

The standard deviation of the pressure coefficient $\sigma_{C_p}(x)$ along the upper surface in Fig. 43 is significantly underpredicted in the shock region by SSC-ENO with a maximum of $\sigma_{C_p,\text{max}} = 0.362$ for $n_s = 50$. It converges only slowly to the SSC-SR solution of $\sigma_{C_p,\text{max}} = 0.616$ at $n_s = 50$, which corresponds to an underprediction by 41.2%. In contrast, the SSC-SR method already gives an accurate prediction for only $n_s = 5$ samples that largely coincides with the approximation of $n_s = 50$. On the other hand, the region around the shock wave in which $\sigma_{C_p}(x)$ is elevated is overpredicted by SSC-ENO. Both effects are caused by the underresolution of the discontinuity in the probability space by the piecewise linear approximation of the discontinuity by SSC-ENO. The linear function leads to a lower standard deviation through the underprediction of the gradients in the response surface and to a longer shock region through the smearing of the discontinuity in the probability space. The normal input distributions increase these two effects due to the concentration of the probability in a small region of the probability space, which makes the sharp resolution of the discontinuity in that region even more important.

The mean $\mu_p(x, y)$ and standard deviation $\sigma_p(x, y)$ of the pressure field around the RAE 2822 airfoil are given in Figs. 44 and 45 for SSC-ENO and SSC-SR with $n_s = 5$ samples, which correspond on the upper surface with the results of Figs. 42 and 43. SSC-ENO does not resolve the smearing of the shock wave in the mean for $n_s = 5$ compared to the deterministic solution of Fig. 39(a) as SSC-SR does. For this minimal number of samples, SSC-SR also captures already the detailed spatial structure of the local standard deviation field $\sigma_p(x, y)$, while SSC-ENO gives a qualitative indication of the region with increased values of $\sigma_p(x, y)$ only.

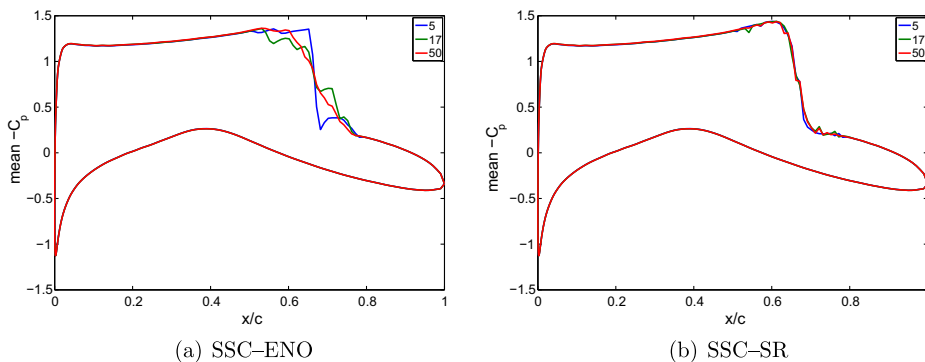


Fig. 42. Mean pressure coefficient $\mu_{C_p}(x)$ along the surface with $n_s = \{5, 17, 50\}$ for the transonic flow over the RAE 2822 airfoil with random free-stream Mach number M_∞ and angle of attack α .

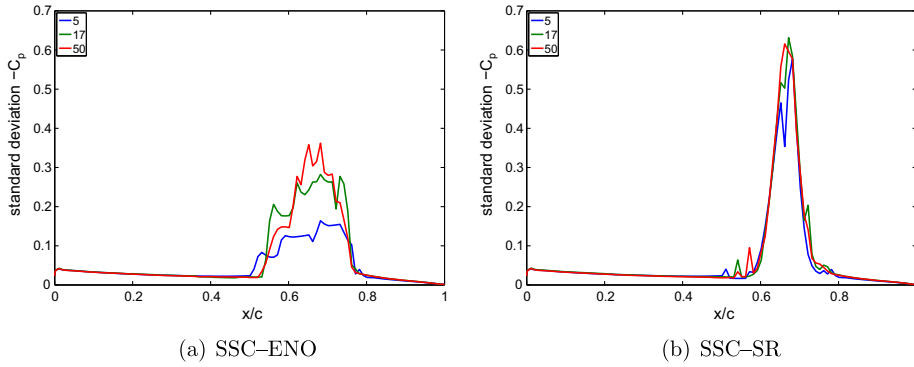


Fig. 43. Standard deviation of the pressure coefficient $\mu_{c_p}(x)$ along the surface with $n_s = \{5, 17, 50\}$ for the transonic flow over the RAE 2822 airfoil with random free-stream Mach number M_∞ and angle of attack α .

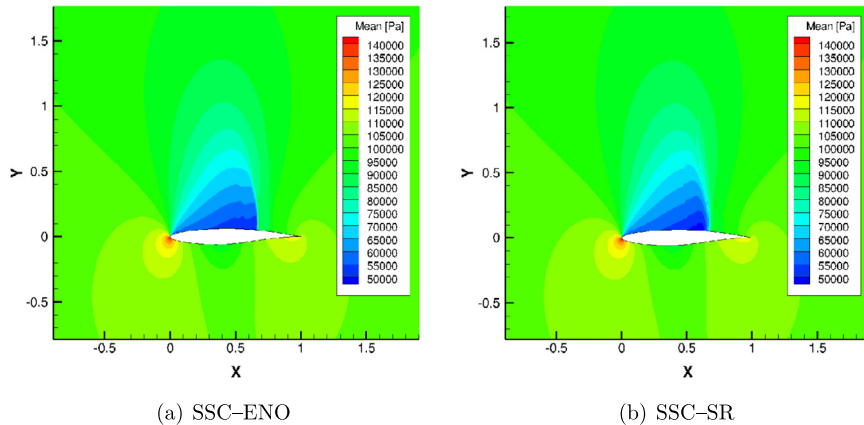


Fig. 44. Mean pressure field $\mu_p(x,y)$ with $n_s = 5$ for the transonic flow over the RAE 2822 airfoil with random free-stream Mach number M_∞ and angle of attack α .

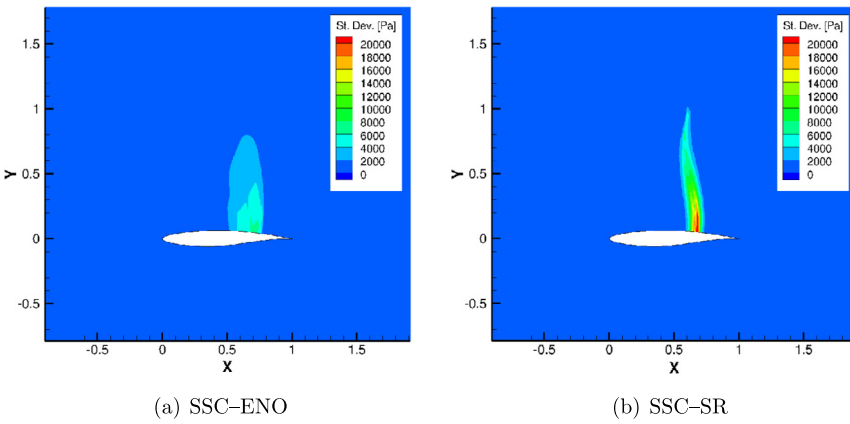


Fig. 45. Standard deviation of the pressure field $\sigma_p(x, y)$ with $n_s = 5$ for the transonic flow over the RAE 2822 airfoil with random free-stream Mach number M_∞ and angle of attack α .

6.2. Comparison with other stochastic methods

In this section, the same results are furnished for MC, PC1, and SC as reported for SSC-ENO and SSC-SR. In order to interpret the Figs. 44 and 45, they are compared with respect to the same contour plots for the other techniques in Fig. 46. Similar

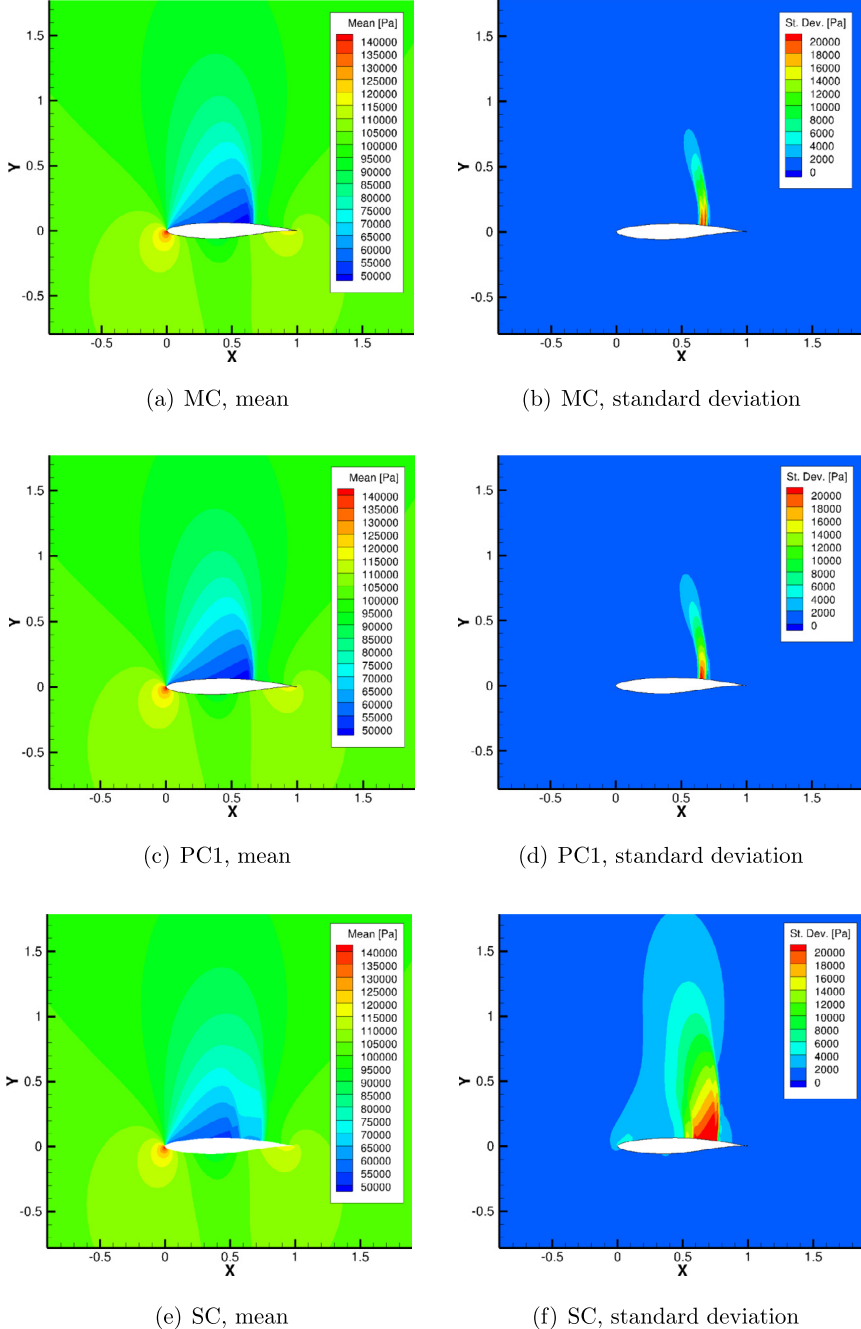


Fig. 46. Pressure field $p(x,y)$ for the MC, PC1, and SC stochastic methods for the transonic flow over the RAE 2822 airfoil with random free-stream Mach number M_∞ and angle of attack α .

results for higher-degree PC are added in the next section. The number of samples for MC and PC1 is equal to the $n_s = 5$ for SSC. The number of samples in SC is $n_s = 4$ based on Clenshaw-Curtis quadrature on the same truncated domain as for SSC.

The largest effect is caused by the truncation of the unbounded domain and the sampling on the boundary of the truncated domain in SC. This results in a significant effect on $\mu_p(x,y)$ and an increase of $\sigma_p(x,y)$ above the entire length of the airfoil. This overprediction is caused by the location of the samples in the tails of the distribution in contrast to the random samples in MC and PC1 near the peak of the distribution. This already affects SSC-ENO to a lesser extent than SC and it is further reduced substantially by the subcell resolution in SSC-SR. The introduction of subcell resolution into SC, PC, and MC could therefore also have the potential to further improve the results of these methods.

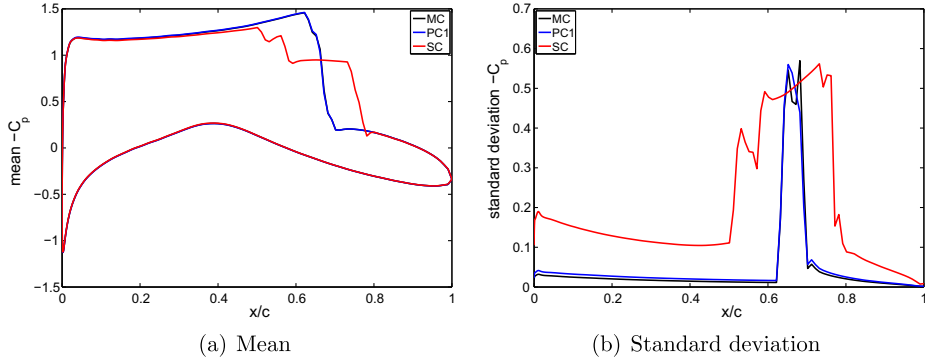


Fig. 47. Pressure coefficient $C_p(x)$ along the surface for the MC, PC1, and SC stochastic methods for the transonic flow over the RAE 2822 airfoil with random free-stream Mach number M_∞ and angle of attack α .

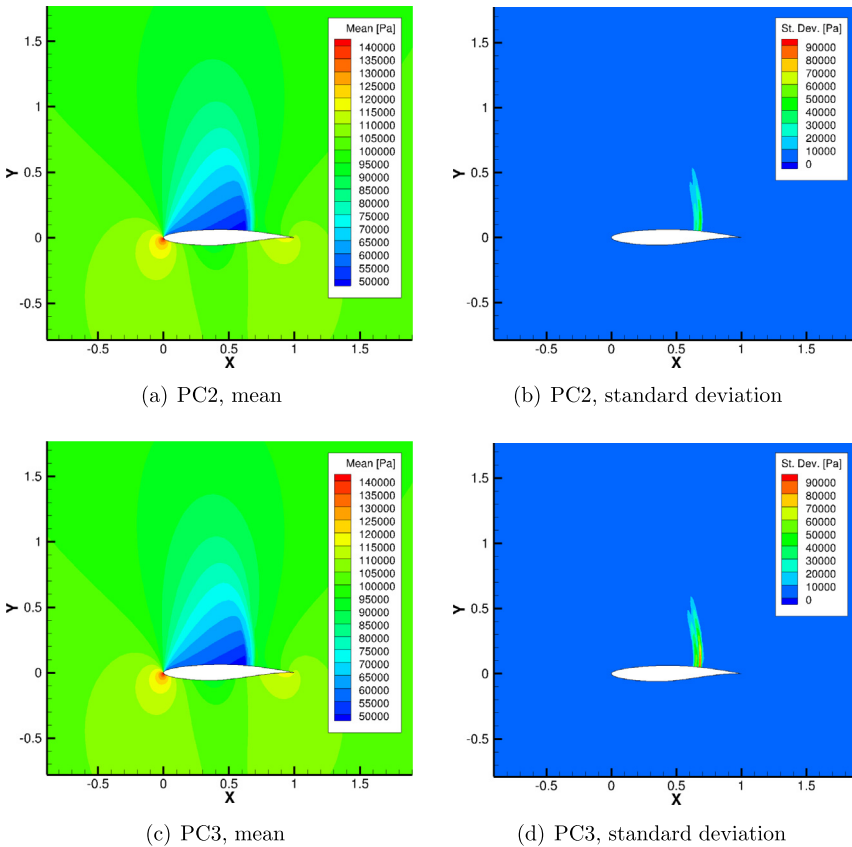


Fig. 48. Pressure field $p(x,y)$ for the higher-degree PC stochastic method for the transonic flow over the RAE 2822 airfoil with random free-stream Mach number M_∞ and angle of attack α .

The corresponding results for the mean and standard deviation of the pressure coefficient are compared in Fig. 47 for the different techniques in particular. SC shows also a large overestimation of $\sigma_{C_p}(x)$ on the surface even in the smooth regions, which would diminish with increasing convergence. On the other hand, MC and PC1 give an underprediction of $\sigma_{C_p,\max}$ at this sample size compared to the final SSC-SR result.

6.3. Higher-degree PC

The global polynomials in higher-degree PC are again not suitable in Fig. 48 for approximating this highly nonlinear problem. This is illustrated by the necessary extension of the maximum of the color-range from $2 \cdot 10^4$ Pa to $9 \cdot 10^4$ Pa as com-

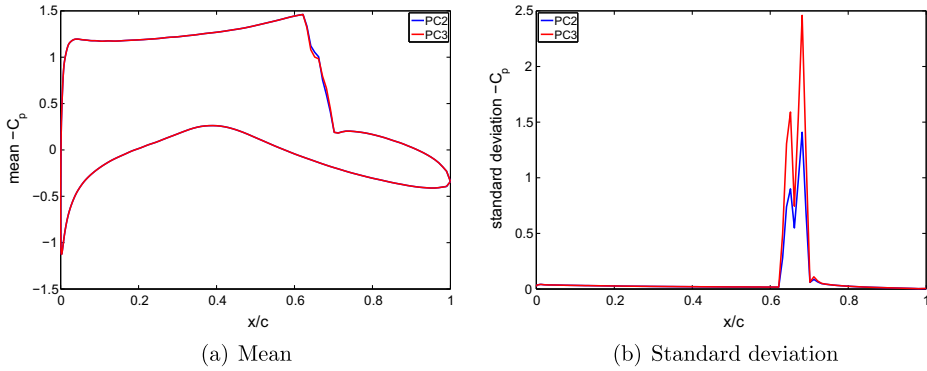


Fig. 49. Pressure coefficient $C_p(x)$ along the surface for the higher-degree PC stochastic method for the transonic flow over the RAE 2822 airfoil with random free-stream Mach number M_∞ and angle of attack α .

pared to Figs. 45 and 46. The maximum for $\sigma_{C_p}(x)$ in Fig. 49 of $\sigma_{C_p,\max} = 2.459$ for PC3 is 4 times larger than for SSC-SR and it increases with p . This even occurs for this case in which the transonic shock wave at the surface is not a true discontinuity but smeared over several spatial cell widths. These results demonstrate the additional value of subcell resolution also under these challenging circumstances.

7. Conclusions

A subcell resolution approach is introduced into the Simplex Stochastic Collocation (SSC) method for solving stochastic problems with randomness in the location of spatial discontinuities. The presented SSC-SR method is based on extracting the discontinuity location $X_{\text{disc}}(\xi)$ in the physical space from each of the deterministic solutions. The realizations of the physical distance $d_{\text{disc}}(\mathbf{x}, \xi)$ to the discontinuity $X_{\text{disc}}(\xi)$ are interpolated over the stochastic dimensions to predict the location of the discontinuity $\Xi_{\text{disc}}(\mathbf{x})$ in the probability space. The stochastic response surface approximations are then extended from both sides up to the discontinuous hypersurface $\Xi_{\text{disc}}(\mathbf{x})$. This results in a truly discontinuous representation of random spatial discontinuities in the interior of the cells discretizing the stochastic dimensions.

The application to a linear advection problem shows that SSC-SR avoids the staircase approximation of the mean and the standard deviation by the SSC-ENO method without subcell resolution, because of the continuous dependence of the discontinuity location $\Xi_{\text{disc}}(\mathbf{x})$ in the probability space on the spatial coordinates \mathbf{x} . It also prevents the underestimation of the maximum standard deviation by matching the exact solution already for the initial number of samples in multiple stochastic and spatial dimensions. The results of the SSC-SR sampling strategy for the Burgers' equation with discontinuities and discontinuous derivatives in the response surface demonstrate that the error convergence of SSC-SR significantly exceeds the first-order accuracy of SSC-ENO. The subcell resolution obtains a piecewise higher-degree approximation of the curved discontinuity with varying strength in the probability space.

In the shock tube problem with random initial conditions, SSC-SR results in a converged solution for $n_s = 15$ samples compared to an underprediction of the maximum standard deviation $\sigma_{p,\max}$ by 4.16% for SSC-ENO with $n_s = 100$. The impact of the random free-stream conditions on the transonic flow around the RAE 2822 airfoil are accurately resolved in the surface pressure distribution, and the mean and standard deviation pressure fields for a minimal number of $n_s = 5$ samples. The non-uniform input probability distributions lead to an even more significant underprediction of $\sigma_{C_p,\max}$ by 41.2% for SSC-ENO with $n_s = 50$.

In future work, the application of the proposed method will be extended to more complex discontinuity surfaces with change of local curvatures, closed topologies, and shock interactions, see for example [17]. SSC-SR resolves discontinuities in the stochastic space due to discontinuous solutions in the physical space by identifying discontinuities. The limits of applicability due to the discontinuity identification are specified below. Most of the problems considered here involve discontinuities of which the location is tracked from its initial position to a certain time. Maybe a more important case is when the discontinuity is generated at a random position from a continuous initial solution. Applications with discontinuities generated by continuous initial conditions will be considered in future work. The steady RAE 2822 airfoil is similar to this case in space in the sense that only at some locations the discontinuity is present and not at others. This identification problem also needs to be considered in the light of resolving high-gradient problems in the form of the viscous counterpart of the presented test cases. It may not be possible to define the point of the discontinuity location for these problems with smeared discontinuities. Instead, the point of the highest gradient can be used such as in the cases with numerical diffusion in the FVM spatial discretizations in this work. SSC-SR has been shown to converge for these problems with numerical viscosity. An explicit modeling of the gradient in the response surface could be considered next if the regularity properties of the solution are known a priori. Whether the origin of the smearing is physical or numerical is expected to be similar from a purely stochastic discretization perspective. SSC-SR has also been shown to converge for problems with numerical viscosity, since

the strength of the inserted discontinuity in the response surface will eventually vanish when the samples are drawn from a smooth response. The original deterministic subcell resolution for the FVM spatial discretization is also known to converge the jump size to the level of the reconstruction error if a discontinuity is placed in a smooth part of the solution [13]. The interpolation algorithm can automatically treat an arbitrary number of spatial discontinuities or discontinuous derivatives after they are extracted and categorized by an appropriate shock sensor.

Acknowledgments

This work was supported by the Netherlands Organization for Scientific Research (NWO) and the European Union Marie Curie Cofund Action under Rubicon grant 680–50–1002.

Appendix A. Simplex stochastic collocation with stencil selection

The SSC method [34,35] starts with an initial discretization of the probability space consisting of a simplex tessellation of the sampling points ξ_k at the corners of the hypercube parameter space Ξ and one ξ_k at the nominal input values for ξ . The approximation is then refined by splitting the longest edge of a simplex Ξ_j in two by adding a sampling point ξ_k . The random sampling point is located at least one third of the edge length away from the endpoints to ensure a sufficient spread of the samples. The tessellation is updated by a Delaunay triangulation of the new set of sampling points ξ_k or the simplexes Ξ_j that contain the refined edge can all be split in two. In a one-dimensional probability space, the new sampling point ξ_k is used to split the cell Ξ_j into two cells of equal size.

The interpolation $w(\mathbf{x}, \xi)$ is based on a stencil $S_j(\mathbf{x})$ of $N_j(\mathbf{x}) + 1 = P_j(\mathbf{x}) + 1$ sampling points ξ_k . The stencil size at an \mathbf{x} -location is restricted by the available number of samples $N_j(\mathbf{x}) + 1 \leq n_s$ and the Local Extremum Conserving (LEC) limiter [35] for the polynomial degree $p_j(\mathbf{x})$ given by

$$\min_{\xi \in \Xi_i} w_i(\mathbf{x}, \xi) = \min \mathbf{v}_i(\mathbf{x}) \wedge \max_{\xi \in \Xi_i} w_i(\mathbf{x}, \xi) = \max \mathbf{v}_i(\mathbf{x}), \quad (\text{A.1})$$

in all simplexes Ξ_i that are contained in the stencil $S_j(\mathbf{x})$ of the simplex Ξ_j , with $\mathbf{v}_i(\mathbf{x}) = \{v_{k_{i,0}}(\mathbf{x}), \dots, v_{k_{i,n_s}}(\mathbf{x})\}$ the samples $v_k(\mathbf{x})$ at the vertexes ξ_k of the simplex Ξ_i . In the subcell resolution formulation, the stencils $S_j(\mathbf{x})$ are also explicitly restrained from crossing the discontinuity location $\Xi_{\text{disc}}(\mathbf{x})$ in the probability space.

The sampling points ξ_k are added to the stencil $S_j(\mathbf{x})$ in the order of their Euclidean distance to the center of simplex Ξ_j in the parameter space Ξ . In the extension to the SSC-ENO method [36] with ENO-type stencil selection, the simplex Ξ_j is assigned the nearest neighbor stencil $S_i(\mathbf{x})$ of another simplex Ξ_i , if its polynomial degree $p_i(\mathbf{x})$ is higher than that of $S_j(\mathbf{x})$ and if $S_i(\mathbf{x})$ contains Ξ_j . The stencil selection leads to higher-degree interpolations $w_j(\mathbf{x}, \xi)$ in the cells Ξ_j next to the discontinuous simplexes, which are used in the subcell resolution approach for the extrapolation. The moments $\mu_{u_i}(\mathbf{x})$ of the response $u(\mathbf{x}, \xi)$ are finally approximated by integrating the function $w(\mathbf{x}, \xi)$ over the parameter space Ξ using a Monte Carlo evaluation with $n_{mc} \gg n_s$ integration points ξ_{mc_k}

$$\mu_{u_i}(\mathbf{x}) \approx \sum_{j=1}^{n_e} \int_{\Xi_j} w_j(\mathbf{x}, \xi)^i f_\xi(\xi) d\xi \approx \sum_{k=1}^{n_{mc}} w(\mathbf{x}, \xi_{mc_k})^i, \quad (\text{A.2})$$

with $w(\mathbf{x}, \xi_{mc_k}) = w_j(\mathbf{x}, \xi_{mc_k})$ for $\xi_{mc_k} \in \Xi_j$.

Appendix B. Subcell resolution for discontinuous derivatives

Discontinuities in the first derivatives of a continuous response surface $u(x, \xi)$ can also be treated by the subcell resolution algorithm to avoid a local reduction in the polynomial degree p_j of the approximation $w(x, \xi)$. The extraction step $\mathbf{v}_{\text{disc}} = \mathcal{E}(\mathbf{v}(x))$ determines, in that case, the realizations \mathbf{v}_{disc} of the location of the discontinuous derivatives in the physical space. A method \mathcal{E} for detecting kinks in the samples $\mathbf{v}(x)$ is illustrated for the examples in Sections 4 and 5. The interpolation $w_{\text{disc}}(\xi)$ of the realizations \mathbf{v}_{disc} is then used to determine the hypersurface $\Xi_{\text{disc}}(x)$ describing the location of the discontinuous derivatives in the probability space in order to construct the different approximations $w_j^-(x, \xi)$ and $w_j^+(x, \xi)$ in the simplexes Ξ_j that contain $\Xi_{\text{disc}}(x)$ as in (5). This leads to a response surface approximation $w(x, \xi)$ with discontinuous derivatives at $\Xi_{\text{disc}}(x)$, which is however not necessarily continuous at $\Xi_{\text{disc}}(x)$. The size of this, in general small, discontinuity at $\Xi_{\text{disc}}(x)$ decreases with an increasingly accurate approximation of the smooth responses on both sides of $\Xi_{\text{disc}}(x)$ as the number of samples n_s increases. An example with a discontinuous derivative in a one-dimensional probability space is given in Fig. B.50, which is equivalent to the discontinuous example in Fig. 4(a) and (c). Fig. 4(b) would be the same for both cases.

In the case that $\Xi_{\text{disc}}(x)$ represents a discontinuous derivative and no Ξ_j^- is available for updating $w_j^-(x, \xi)$ in $\Xi_j^-(x)$, because $\Xi_{\text{disc}}(x)$ is located close to the boundary of Ξ , then a linear function is used for $w_j^-(x, \xi)$, instead of a constant value in case $\Xi_{\text{disc}}(x)$ is a discontinuity. The updated interpolation $w_j^+(x, \xi)$ in $\Xi_j^+(x)$ on the other side of $\Xi_{\text{disc}}(x)$ can be used in combination with the continuity of $u(x, \xi)$ at $\Xi_{\text{disc}}(x)$ to update $w_j^-(x, \xi)$ using a linear approximation. The first step is then to determine the values of $w_j^+(x, \xi)$ at the locations where $\Xi_{\text{disc}}(x)$ intersects the edges of Ξ_j . These values are used in combina-

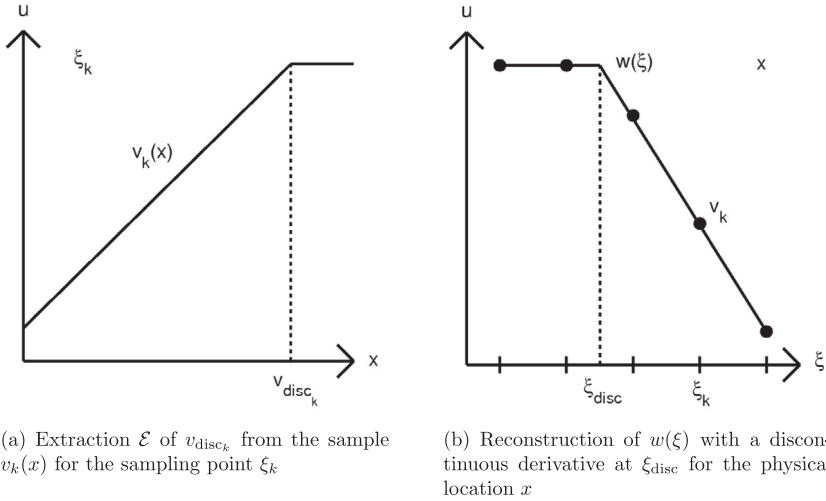


Fig. B.50. Example of the subcell resolution approach for a discontinuous derivative in a one-dimensional probability space.

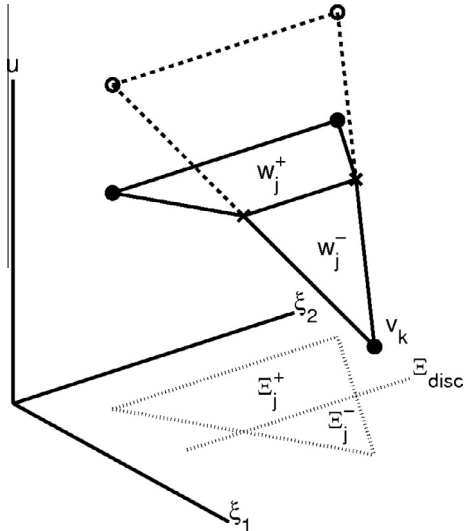


Fig. B.51. Subcell resolution for a discontinuous derivative $\Xi_{disc}(x)$ located close to the boundary of a two-dimensional parameter space Ξ with a linear update of $w_j^-(x, \xi)$ using $w_j^+(x, \xi)$ and the continuity at $\Xi_{disc}(x)$.

tion with the samples $v_k(x)$ at the vertexes ξ_k of Ξ_j in Ξ_j^- to construct virtual values in the other vertexes of Ξ_j by linear extrapolation over the edges. This is visualized in Fig. B.51 by the open circles in the approximation of the response $u(x, \xi)$ in a two-dimensional probability space. The virtual values are used together with $v_k(x)$ at the vertexes ξ_k in Ξ_j^- to construct a linear update for $w_j^-(x, \xi)$ using (2) with $p_j = 1$. If multiple virtual values are estimated for one vertex, because the vertex in Ξ_j^+ is the endpoint of multiple edges of Ξ_j that cross $\Xi_{disc}(x)$, then their arithmetic average is used.

References

- [1] R. Abgrall, P.M. Congedo, A semi-intrusive deterministic approach to uncertainty quantification in non-linear fluid flow problems, *J. Comput. Phys.* 235 (2013) 828–845.
- [2] R. Abgrall, A simple, flexible and generic deterministic approach to uncertainty quantifications in nonlinear problems: application to fluid flow problems, 5th European Conference on Computational Fluid Dynamics, ECCOMAS CFD, Lisbon, Portugal, 2010.
- [3] N. Agarwal, N.R. Aluru, A domain adaptive stochastic collocation approach for analysis of MEMS under uncertainty, *J. Comput. Phys.* 228 (2009) 7662–7688.
- [4] I. Babuška, R. Tempone, G.E. Zouraris, Galerkin finite elements approximation of stochastic finite elements, *SIAM J. Numer. Anal.* 42 (2004) 800–825.
- [5] I. Babuška, F. Nobile, R. Tempone, A stochastic collocation method for elliptic partial differential equations with random input data, *SIAM J. Numer. Anal.* 45 (2007) 1005–1034.

- [6] T. Barth, On the propagation of statistical model parameter uncertainty in CFD calculations, *Theor. Comput. Fluid Dyn.*, DOI: 10.1007/s00162-011-0221-2.
- [7] T. Barth, UQ methods for nonlinear conservation laws containing discontinuities, *AVT-193 Lecture Series on Uncertainty Quantification, RTO-AVT-VKI Short Course on Uncertainty Quantification, California, Stanford*, 2011.
- [8] T. Chantrasmi, A. Doostan, G. Iaccarino, Padé-Legendre approximants for uncertainty analysis with discontinuous response surfaces, *J. Comput. Phys.* 228 (2009) 7159–7180.
- [9] J.-C. Chassaing, D. Lucor, Stochastic investigation of flows about airfoils at transonic speeds, *AIAA J.* 48 (2010) 938–950.
- [10] Q.-Y. Chen, D. Gottlieb, J.S. Hesthaven, Uncertainty analysis for the steady-state flows in a dual throat nozzle, *J. Comput. Phys.* 204 (2005) 378–398.
- [11] P.H. Cook, M.A. McDonald, M.C.P. Firmin, Aerofoil RAE 2822 pressure distributions, and boundary layer and wake measurements, *Experimental Data Base for Computer Program Assessment, AGARD Report AR 138*, 1979.
- [12] A. Harten, S. Osher, Uniformly high-order accurate nonoscillatory schemes I, *SIAM J. Numer. Anal.* 24 (1987) 279–309.
- [13] A. Harten, ENO schemes with subcell resolution, *J. Comput. Phys.* 83 (1989) 148–184.
- [14] J. Foo, X. Wan, G.E. Karniadakis, The multi-element probabilistic collocation method (ME-PCM): Error analysis and applications, *J. Comput. Phys.* 227 (2008) 9572–9595.
- [15] R.G. Ghanem, P.D. Spanos, *Stochastic Finite Elements: A Spectral Approach*, Springer-Verlag, New York, 1991.
- [16] D. Ghosh, R. Ghanem, Stochastic convergence acceleration through basis enrichment of polynomial chaos expansions, *Int. J. Numer. Meth. Eng.* 73 (2008) 162–184.
- [17] D. Lucor, J. Witteveen, P. Constantine, D. Schiazzoli, G. Iaccarino, Comparison of adaptive uncertainty quantification approaches for shock wave-dominated flows, *Proceedings of the Summer Program, Center for Turbulence Research, Stanford University* (2012) 219–228.
- [18] X. Ma, N. Zabaras, An adaptive hierarchical sparse grid collocation algorithm for the solution of stochastic differential equations, *J. Comput. Phys.* 228 (2009) 3084–3113.
- [19] O.P. Le Maître, H.N. Najm, R.G. Ghanem, O.M. Knio, Multi-resolution analysis of Wiener-type uncertainty propagation schemes, *J. Comput. Phys.* 197 (2004) 502–531.
- [20] L. Mathelin, O.P. Le Maître, Dual-based a posteriori error estimate for stochastic finite element methods, *Commun. Appl. Math. Comput. Sci.* 2 (2007) 83–115.
- [21] G. Onorato, G.J.A. Loeven, G. Ghorbaniasl, H. Bijl, C. Lacor, Comparison of intrusive and non-intrusive polynomial chaos methods for CFD applications in aeronautics, *European Conference on Computational Fluid Dynamics, ECCOMAS CFD 2010, Lisbon, Portugal*, 2010.
- [22] P. Pettersson, G. Iaccarino, J. Nordström, Numerical analysis of the Burgers' equation in the presence of uncertainty, *J. Comput. Phys.* 228 (2009) 8394–8412.
- [23] G. Poëtte, B. Després, D. Lucor, Uncertainty quantification for systems of conservation laws, *J. Comput. Phys.* 228 (2009) 2443–2467.
- [24] F.H. Post, B. Vrolijk, H. Hauser, R.S. Laramee, H. Doleisch, The state of the art in flow visualisation: feature extraction and tracking, *Computer Graphics Forum* 22 (2003) (2003) 775–792.
- [25] M.T. Reagan, H.N. Najm, R.G. Ghanem, O.M. Knio, Uncertainty quantification in reacting-flow simulations through non-intrusive spectral projection, *Combust. Flame* 132 (2003) 545–555.
- [26] F. Simon, P. Guillen, P. Sagaut, D. Lucor, A gPC-based approach to uncertain transonic aerodynamics, *Comput. Methods Appl. Mech. Eng.* 199 (2010) 1091–1099.
- [27] E.F. Toro, *Riemann Solvers and Numerical Methods for Fluid Dynamics*, Springer-Verlag, Berlin, 1997.
- [28] J. Tryoen, O. Le Maître, M. Ndjinga, A. Ern, Intrusive Galerkin methods with upwinding for uncertain nonlinear hyperbolic systems, *J. Comput. Phys.* 229 (2010) 6485–6511.
- [29] J. Tryoen, O. Le Maître, A. Ern, Adaptive anisotropic spectral stochastic methods for uncertain scalar conservation laws, *SIAM J. Sci. Comput.* 34 (2012) A2459–A2481.
- [30] X. Wan, G.E. Karniadakis, An adaptive multi-element generalized polynomial chaos method for stochastic differential equations, *J. Comput. Phys.* 209 (2005) 617–642.
- [31] J.A.S. Witteveen, H. Bijl, A TVD uncertainty quantification method with bounded error applied to transonic airfoil flutter, *Commun. Comput. Phys.* 6 (2009) 406–432.
- [32] J.A.S. Witteveen, G.J.A. Loeven, H. Bijl, An adaptive stochastic finite elements approach based on Newton–Cotes quadrature in simplex elements, *Comput. Fluids* 38 (2009) 1270–1288.
- [33] J.A.S. Witteveen, Second order front tracking for the Euler equations, *J. Comput. Phys.* 229 (2010) 2719–2739.
- [34] J.A.S. Witteveen, G. Iaccarino, Simplex stochastic collocation with random sampling and extrapolation for nonhypercube probability spaces, *SIAM J. Sci. Comput.* 34 (2012) A814–A838.
- [35] J.A.S. Witteveen, G. Iaccarino, Refinement criteria for simplex stochastic collocation with local extremum diminishing robustness, *SIAM J. Sci. Comput.* 34 (2012) A1522–A1543.
- [36] J.A.S. Witteveen, G. Iaccarino, Simplex stochastic collocation with ENO-type stencil selection for robust uncertainty quantification, *J. Comput. Phys.* 239 (2013) 1–21.
- [37] D. Xiu, G.E. Karniadakis, The Wiener–Askey polynomial chaos for stochastic differential equations, *SIAM J. Sci. Comput.* 24 (2002) 619–644.
- [38] D. Xiu, J.S. Hesthaven, High-order collocation methods for differential equations with random inputs, *SIAM J. Sci. Comput.* 27 (2005) 1118–1139.